

Laser Induced Fluorescence in atmospheric pressure discharges

G. Dilecce^{1,2‡}, L. M. Martini², P. Tosi², M. Scotoni² and S. De Benedictis¹

¹Istituto di Metodologie Inorganiche e dei Plasmi-CNR, Via Orabona 4, 70125 Bari - ITALY

²Dipartimento di Fisica Università di Trento, Via Sommarive 14, 38123 Povo - Trento - ITALY

Abstract.

This paper offers an outline of Laser Induced Fluorescence (LIF) diagnostics and practical recommendations for its use in atmospheric pressure discharges. LIF principles, technical requirements and rationalization of experimental outcomes by modelling are addressed. Important issues that are particularly relevant to small scale, spatially inhomogeneous discharges, like plasma-jets, are emphasized. For the first time, all collision processes and the spatial non-homogeneity of the laser beam are together accounted for in the LIF model. Saturation characteristics are discussed and used for the assessment of model parameters. A calibration procedure is discussed and implemented. Gas temperature measurements by LIF are also addressed. The whole description of the technique is given, without loss of generality, through the example of its application to the OH radical. Notes on other diatomic radicals, CH, NO and CN, are given along the paper. Some results in a RF plasma-jet are presented as an example of application in a discharge system where all the concepts developed in the paper are applied.

1. Introduction

Critical requirements for the detection of transient species in atmospheric pressure (ATP) discharges are sensitivity, time and space resolution. This is particularly true in plasma jets flowing towards a humid target. Atmospheric pressure plasma jets [1, 2] are widely used in Plasma Medicine issues [3]. The gas mixture composition and the physics of the discharge strongly depend on the presence of the target, and local discharge conditions change in a sub-mm space scale. In addition the voltage source excitation is often pulsed.

Laser Induced Fluorescence (LIF) is the technique that satisfies these needs. LIF (see the recent review [4] on LIF at atmospheric pressure) is based upon the absorption of

‡ corresponding author: giorgio.dilecce@imip.cnr.it

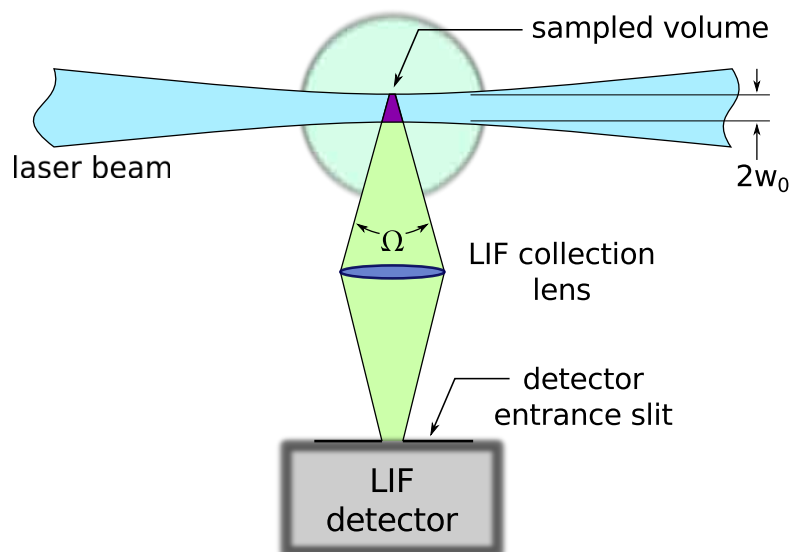


Figure 1. Typical geometry of the LIF experiment.

laser photons by a molecular lower state, the state to be probed, and on the observation of light (fluorescence) emitted by an upper state. In single-photon LIF the upper and lower states are linked by a dipole-allowed ro-vibronic transition which the laser is tuned to. The observable is then a complex function of both the absorption rate and the collision and radiative properties of the upper state. At atmospheric pressure, collision processes - electronic quenching (Q), vibrational (VET) and rotational (RET) energy transfers - deeply influence the fluorescence outcome and must be duly taken into account to rationalize LIF measurements. The spatial resolution of LIF is determined by the geometry of the experiment. The optical axis of the fluorescence detection arrangement is usually perpendicular to the laser beam, and the relevant collection optics includes a slit or an iris imaged onto the sampled region by a lens assembly. The sampled volume is the intersection of the slit/iris image with the laser beam. It can typically be a cylinder with diameter and height of the order of 0.1 mm with a focused laser beam (see Figure 1). The temporal resolution is achieved by pulsed tuneable lasers, and is determined by the pulse duration, that is of the order of 10 ns. This is enough to capturing the kinetics in pulsed discharges and in the afterglow of single filament events, but not for tracing the kinetics within single filaments. Both time and space resolutions of LIF are suitable for a detailed characterization of atmospheric pressure plasma jets.

In atmospheric plasmas, single-photon LIF has been applied to CH [5], CN [6], NO [7, 8, 9], OH molecules, with various degrees of accuracy, ranging from simple detection to relative and absolute measurements. The most studied radical is by far the OH molecule. It being a very reactive oxidizing specie, it is important in plasma medicine and plasma assisted combustion issues. Many papers have been recently published on OH quantitative detection by LIF: in a pulsed corona discharge [10, 11, 12, 13, 14], in a DBD [15], in a pulsed DBD [16, 17, 18], in a plasma-jet

[19, 20, 21, 22, 23, 24, 25], in a pulsed discharge over a liquid surface [13], in a pin-to-pin single filament discharge [26, 27, 28], in nanosecond discharges for plasma assisted combustion [29, 30]. Transitions used for OH LIF detection are those of the OH ($X^2\Pi - A^2\Sigma^+$) 3064 Å system. Collision phenomena in the OH(A) state (see par. 5.2) are well known, due to the long lasting interest on this molecule in combustion and atmospheric chemistry research. In addition, the rotational structure of the 3064 Å system bands, with its weakly overlapped branches and widely spaced rotational lines, makes it easy to isolate ro-vibronic lines by medium bandwidth ($\sim 10^{-2}$ Å) lasers. The OH radical is then an ideal molecule for laser spectroscopy, and its measurement in an ATP plasma jet is the ideal arena to present state-of-the-art LIF techniques. In this paper we give a general description of the LIF technique by way of OH absolute measurements in a RF plasma jet. We address in detail the following issues: a) the modelling of the LIF measurement, taking into account RET and VET collisional processes and the spatial non-uniformity of the laser beam; b) saturation characteristics; c) absolute calibration; d) rotational temperature measurements; e) instrumental details. All concepts have general validity and can be applied to any other case of LIF on molecular species. Some measurements in a RF plasma jet are also presented. Details of some experimental features, that we believe to be important for a good experiment, are given in each relevant section in paragraphs labelled “good practice notes”. Readers may initially skip these notes in order to let the reading flow without interruptions.

2. Experimental apparatus

2.1. Laser and optical measurement setup

A block diagram of the LIF apparatus is shown in Figure 2. The laser source is a Quantel TDL50 dye laser pumped by a Quantel YG580 Q-switched Nd:YAG laser. Rhodamine 590 chloride dye is used. The dye laser is operated without amplifier, and the output energy of the oscillator plus pre-amplifier is 11 mJ/pulse. The second harmonic at wavelengths around 281 nm is generated by a KDP crystal. The UV energy is about 0.53 mJ/pulse. The beam is then manipulated by a variable attenuator and a spatial filter. The filtered laser beam is then injected in the target area either directly, with an estimated 2 mm beam diameter, or focused by a $f = 250$ mm UVFS plano-convex lens, with a calculated beam waist of 75 μm .

The fluorescence signal is collected by a $f = 200$ mm, 1 inch UVFS plano-convex lens and fed into a Shamrock 303i, 300 mm focal length monochromator. The monochromator is coupled with two different detectors: a 1024×1024 pixels intensified CCD (ICCD) (DH334T-18U-03, Andor) and a photomultiplier tube (PMT) (8575, Burle Electron Tubes). The PMT signal is measured as the voltage drop on the 50 Ω input resistance of a digital oscilloscope (Agilent Infiniium 54831B, 600 MHz 4 Gsps). The synchronization of the laser firing, acquisition systems and pulsed discharges is obtained via a five-channels digital delay generator (DDG). Further details will be given along

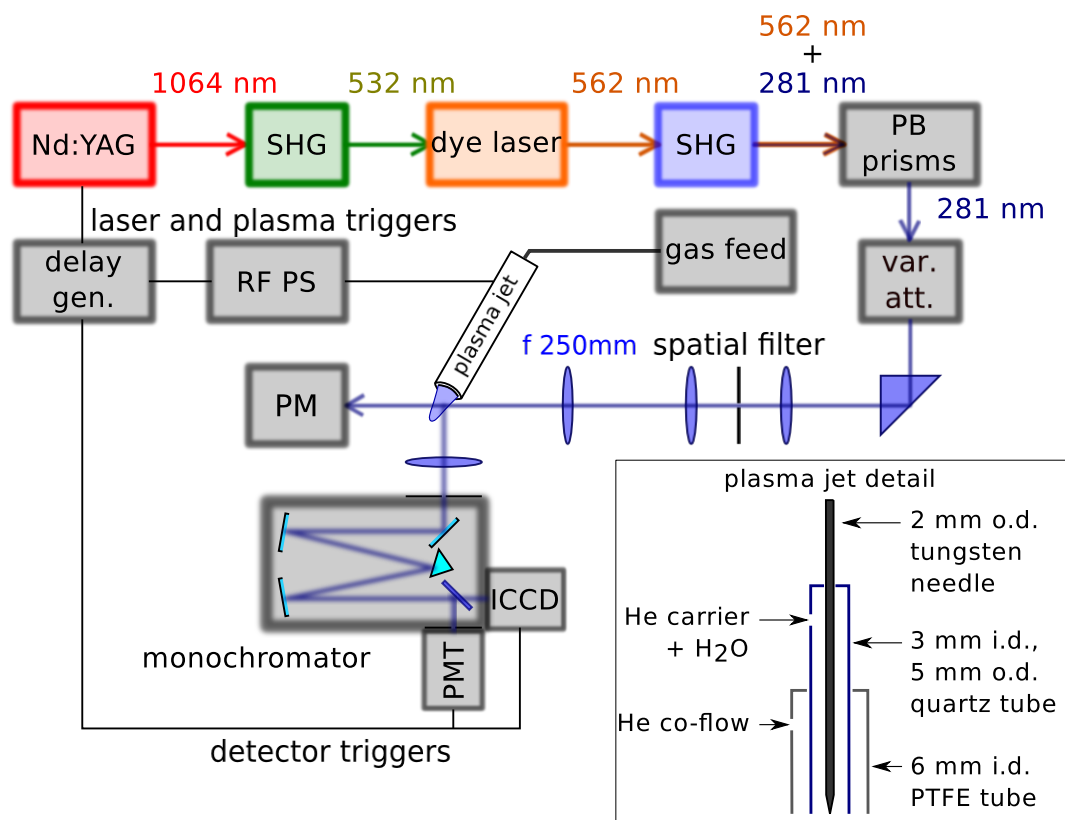


Figure 2. Block diagram of the experimental apparatus. Details of the plasma-jet alone are drawn in the right-bottom box.

the text when their importance will be made clear.

2.2. RF plasma jet

The schematic representation of the RF-driven plasma jet is given in the box in Figure 2. The plasma source consists of a tungsten needle of 2 mm diameter that acts as high voltage electrode, surrounded by a quartz tube (3 mm inner diameter, 5 mm outer diameter) where a mixture of He and H₂O flows. In order to reduce the contamination of plasma plume by the outside atmosphere, a PTFE tube (6 mm inner diameter) concentric to the needle is used to inject a co-flow of pure He. The He-H₂O mixture is obtained by injecting a fraction of the gas carrier inside a bubbler filled with distilled water at room temperature. Gas flows are controlled by three mass flow controllers (1179A, MKS). A grounded electrode (an aluminium cylinder of 20 mm diameter) is placed 11 mm below the tungsten needle tip. Liquid targets can be placed above the grounded electrode inside a small PTFE cylindrical vessel (150 mm³ volume, 1.2 mm thick). In this configuration the plasma jet is a so-called linear field plasma jet, because the electric field and the gas flow have the same direction [31]. A 500 W RF power supply (RF5S, RFPP) working at 13.56 MHz is used to generate the discharge. Impedance matching between the power supply and the plasma jet is achieved placing an automatic

matching network (AM5, RFPP) between them. The power dissipated in the plasma is measured by a voltage probe (P6015A, Tektronix) and a high bandwidth (200 Hz to 500 MHz) I/V converter (CT-C1.0, Magnelab). Probes output signals are recorded and digitalised by a Digital Storage Oscilloscope (LeCroy Wavesurfer 104MXs-A 1 GHz 5 GSps). The power dissipated by the plasma jet is calculated by integration of the voltage times the current, by taking into account propagation delays in the cables connecting the probes to the oscilloscope. Propagation delays are determined by connecting a purely capacitive load (a vacuum capacitor) to the probes and then comparing the measured value of impedance to the expected one [32]. The actual power dissipated into the plasma is calculated as the difference between power values measured in discharge on and off condition (i.e. with and without gas, respectively) at the same current flowing into the plasma jet [33].

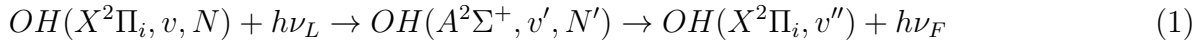
2.3. Calibration cell

The calibration cell is the parallel plates dielectric barrier discharge described in [34]. Its geometry is composed of two 35×35 mm² electrodes covered by 0.7 mm thick alumina plates and separated by a 4.5 mm gap. The gas feed system is the same as that of the RF jet. The discharge voltage is sinusoidal at 20 kHz. OH density was measured in [34] at various conditions of gas mixture and discharge power by time-resolved broad-band absorption spectroscopy (TR-BBAS) [35] with a 25% error. Some of those conditions have been selected here for LIF calibration.

3. OH LIF Spectroscopy

3.1. Spectroscopic scheme

We adopted the classical excitation-detection scheme that involves transitions of the 3064 Å system (as in [17]):



with $v = 0$, $v'' = v' = 1$, $i=1/2, 3/2$. The total angular momentum quantum number is $J=N+1/2$ for $i=3/2$ and $J=N-1/2$ for $i=1/2$, where N is the quantum number of the total angular momentum excluding electron spin § We used several choices of rotational transitions. The $Q_1(1)$ at 2819.13 Å used for fixed wavelength measurements of OH density. The $P_1(3)$ at 2830.09 Å used for the recovery of the saturation characteristic. The group of lines $Q_{12}(1)$ at 2829.21 Å, $Q_2(1)$ at 2829.23 Å, $Q_1(6)$ at 2829.27 Å, $Q_{12}(3)$ at 2829.31 Å and $Q_2(3)$ at 2829.37 Å is used for temperature measurements.

§ We adopt here the LIFBASE nomenclature, that is equal to that of ref. [36]. In other publications, like [37, 38], the quantum number of the total angular momentum excluding electron spin is labelled as K , while N is used for the angular momentum of nuclear rotation. In the following we adopt N in parenthesis for the classification of rotational lines.

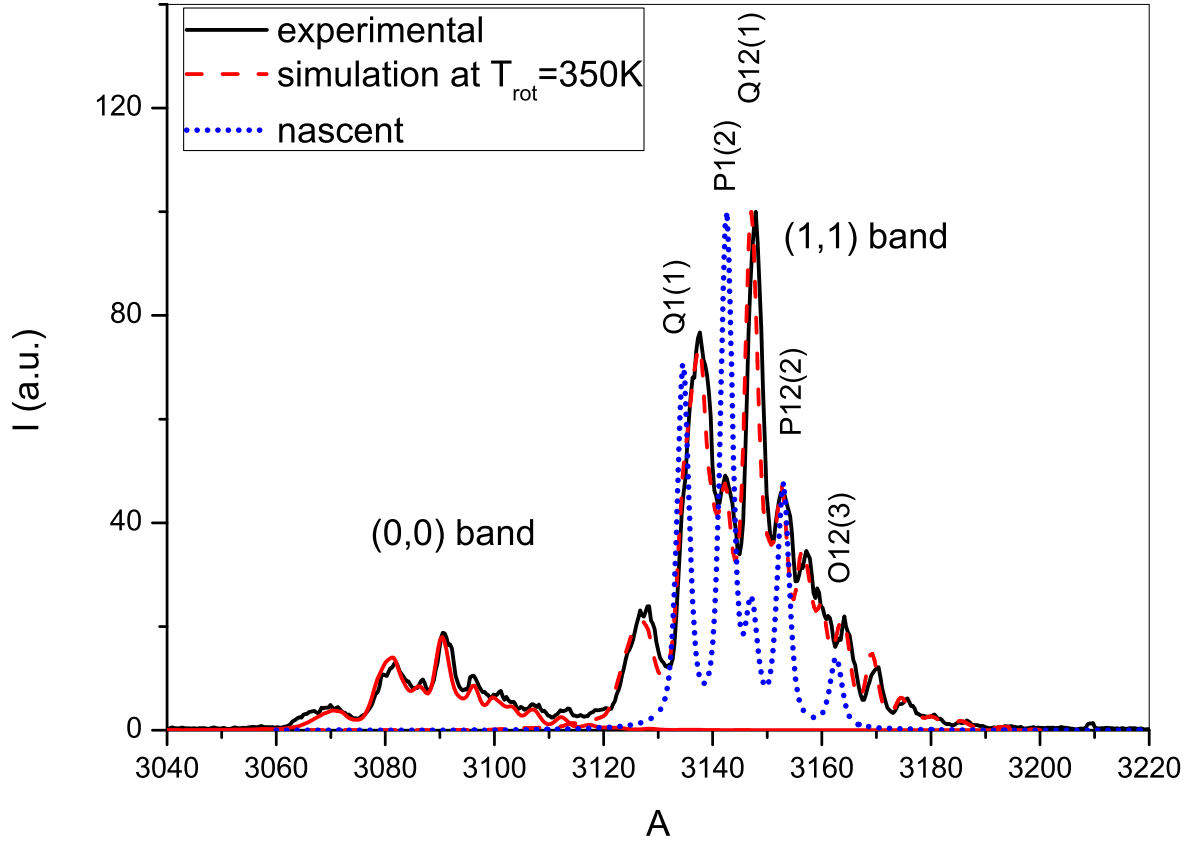


Figure 3. Laser Induced Fluorescence spectrum in a He-H₂O dielectric barrier discharge, after excitation of OH($A^2\Sigma^+$, $v' = 1$, $N' = 1$) by $Q_1(1)$ line. The rotational transitions labels refer to the nascent spectrum.

The fluorescence is captured by a broadband detection. Due to fast RET collisions, the initial population of the rotational level N' excited by the laser is quickly redistributed in the whole rotational manifold towards a Boltzmann distribution at equilibrium with the gas temperature. This can be seen in Figure 3, in which the observed fluorescence spectrum shows a thermalized rotational distribution in contrast to the nascent spectrum (i.e. in the absence of RET collisions) that contains only transitions coming from the $N'=1$ pumped level (details on the spectra simulation and measurements will be given later).

Another clear feature of the spectrum shown in Figure 3 is the presence of the (0,0) vibro-electronic band in spite of the fact that the (1,1) band only has been pumped by the laser. This is due to VET processes induced by collision with water molecules. This issue also will be detailed later.

3.1.1. Notes on absorption spectroscopy of $^2\Sigma - ^2\Pi$ transitions. The $^2\Pi$ ground state rotational is splitted by spin-orbit interaction into two sub-manifold components F_1 ($^2\Pi_{3/2}$, $J=N+1/2$) and F_2 ($^2\Pi_{1/2}$, $J=N-1/2$). Λ -doubling further splits the components into $+/-$ sublevels. This determines four rotational sub-manifolds F_1 , F_2 and F'_1 , F'_2 [37],

which can also be classified according to notation “e,f” parity. The latter choice makes the notation independent of the coupling case [39], with labels $F_{1e}(N)$ and $F_{1f}(N)$, and $F_{2e}(N)$ and $F_{2f}(N)$ respectively for ${}^2\Pi_{3/2}$ and ${}^2\Pi_{1/2}$ sub-states. Analogous notations are used for the ${}^2\Sigma$ state although $\Lambda = 0$ and no Λ -doubling occurs. No line doublets appear due to the selection rule according to which *positive terms combine only with negative and vice versa* (see [37], p. 241 and 257-259. Note that in [37] the F_1 , F_2 notations are reversed), or equivalently $e \leftrightarrow e$ and $f \leftrightarrow f$ transitions are allowed for $\Delta J = \pm 1$ branches, while $e \leftrightarrow f$ are allowed for the $\Delta J = 0$ branch [39]. Since the Λ energy splitting is very small, the populations of the two sublevels are identical, and thus equal to one half of the $F(N)$ population. Then, since only one of the two +/- or e/f sublevels is active in the absorption process, one half of the rotational level population must be considered. This fact has been sometimes neglected in LIF and absorption experiments on OH, as it has been pointed out in [40], where a factor of two correction to the previous absorption measurements [41] was applied. The same correction must also be applied to the OH concentration measured by our group by time-resolved broad band absorption [35, 34], in which we erroneously used the total rotational population of F_1 ($N=2$, $J=2.5$), calculated by LIFBASE, for the normalization of the absorption spectra, instead of the $F_{1e}(N=2, J=2.5)$ component. The LIF measurements of [16, 42], that are calibrated by absorption, must then also be multiplied by two.

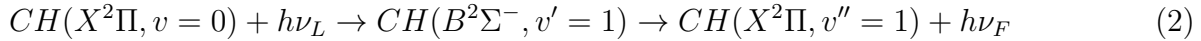
3.1.2. Good practice notes. The detection using a band different from that used for laser absorption is useful for spectral separation of fluorescence from laser light scattered by the apparatus hardware. At ATP this is mandatory since scattered light is abundant because of the small dimension of high pressure discharges. Also, due to electronic quenching, the fluorescence pulse can be very short, with a duration comparable to that of the laser pulse. Time separation of fluorescence from scattered laser light is then impossible. In the specific case of OH, this choice implies the appearance of fluorescence bands produced by VET relaxation. This might be seen as a complication, but, as we shall see, knowledge of the relevant rate coefficients opens a further diagnostic opportunity.

The choice of N must be guided by the criteria of maximum population and smooth dependence on the rotational temperature, so that small local changes of the temperature do not influence appreciably the outcome. Low rotational levels generally satisfy these requirements. For example, when using the $Q_1(1)$ line, the relevant sublevel of the ground state is $F_1(N=1)$. Its relative population is 0.196 at 300 K, 0.167 at 350 K and 0.145 at 400 K. In cold pulsed discharges, where the gas temperature remains below 350 K, neglecting temperature variations produces an error within 15%. The situation is even better for sublevel $F_1(N=2)$ that goes from 0.196 at 300 K to 0.161 at 400 K and for $F_1(N=3)$ that ranges from 0.149 to 0.14 in the 300 - 400 K interval, and drops only to 0.127 at 500 K. The choice, for example, of the $P_1(3)$ line for excitation makes the rotational population of the initial state almost constant in a wide temperature range.

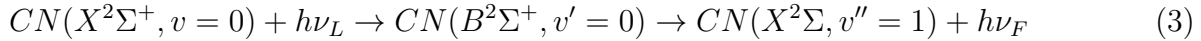
Single line absorption is advisable for the sake of analysis simplicity, especially

if LIF is operated in a partially saturated regime. With common Nd:YAG pumped pulsed dye lasers this is readily achievable in OH. With commercial OPO lasers, that are nowadays quite cheap and feature typical spectral bandwidths of 5 cm^{-1} (about 0.4 \AA at 282 nm), this is not possible. Multi-line absorption can still be reasonably well analysed only in the linear regime.

3.1.3. Other molecules. Schemes for other molecules investigated in ATP discharges are as follows. For the CH radical all the possible transitions involving the three electronic states ($A, B, C \rightarrow X$) are strongly diagonal, limiting the choice of an efficient excitation-detection scheme in which the detected fluorescence band is different from that chosen for laser absorption. The best combination of diagonal/off-diagonal absorption/emission coefficients is given by transitions of the Gerö system [5], with $Q_1(2)$ single line absorption $\lambda=3637.98 \text{ \AA}$:

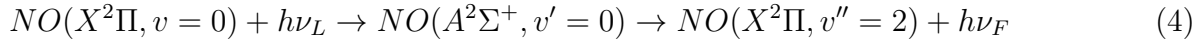


CN detection was achieved in [6] by the following Violet system scheme:



The dense rotational structure of the Violet system bands prevents single lines absorption.

The scheme for NO is quite a classical one, with transitions of the γ -system [7, 8]:



Isolated rotational lines can be found only at high rotational numbers.

3.2. Spectral simulation

Both excitation and fluorescence spectra are simulated by means of the LIFBASE software [43]. The excitation spectrum is that obtained by scanning the laser wavelength with a fixed spectral detection window. The simulated fluorescence spectrum is an emission spectrum with a given rotational distribution. In our case, with full time integration of the fluorescence pulse, we assume a Boltzmann distribution at equilibrium with the gas temperature. The simulation includes Doppler and collisional line broadening. The latter is calculated using the data of [44] in which the absorption broadening of some lines of the (0,0) band has been measured at $T = 300 \text{ K}$ for N_2 , Ar, Ne and He colliders, and assuming that it is similar for the transitions of the (1,0) band. The scaling law:

$$\Delta\nu_c = a \left(\frac{P}{760} \right) \left(\frac{300}{T} \right)^b \quad (5)$$

is used in LIFBASE, with a in cm^{-1} . We have used $b = 0.7$ as for van der Waals interaction potentials [45].

4. Model description

Model calculations of the LIF process are based on a set of rate equations describing the time evolution of the population of the involved states. The applicability of rate equations to coherent light resonant absorption is briefly discussed in the appendix a. Non experts readers can, in the first reading, skip the literature survey.

4.1. Literature survey

The simplest treatment was given in [21], in which the population of the ground state was assumed to be constant, and only the two upper states ($A, v=1$) and ($A, v=0$) were described by rate equations. This approach is valid only in strictly linear regime. The laser pulse was furthermore approximated by a rectangular function of time. With these approximations an analytical solution could be found for the LIF outcome. The same choice was made in [20]. A three level model was implemented in [17] including a rate equation for the ground state and a measured laser pulse time function. The model was solved numerically. Although in principle the three level model includes the possibility to handle saturation effects, it does not account for RET processes in both X and A states that, as we shall see, play an important role in the saturation characteristics. In [46] a fourth level equation for the state ($X, v=1$) was added. This model was taken from [47]. The idea is that electronic quenching of ($A, v=1$) terminates into ($X, v=1$), that is then coupled to the initial ($X, v=0$) state by vibrational relaxation. As a matter of fact, vibrational relaxation in the ground state is slow, and this path is negligible for ($X, v=0$) re-population within the laser duration time. In the same model, electronic quenching of ($A, v=0$) was assumed to terminate the molecule into ($X, v=0$). Although not explicitly stated in that paper, we believe that such an assumption is based on the Franck-Condon factors of the A-X transition, that feature a large prevalence of the (0,0) transition. In [47] a long discussion on this issue is given, without a clear conclusion. Since modelling which fraction of the A state terminates into X state after electronic quenching is quite arbitrary, the authors of [47] calculated the effect of variations of such a fraction on the LIF model outcome. In order to contribute to the process, refilling of the X state by electronic quenching should be competitive with RET refilling, so that its influence to the populations cycle can be important only at very high laser irradiance, when the population of the whole $X, v=0$ rotational manifold starts to be significantly decreased within the laser pulse duration. For this reason we decided to neglect this process, as well as the slow radiative refilling, in the model we describe in the next section. RET collisions were considered also in [48] and [47]. The six-level model of [47] was also used in [49]. In this model the two ro-vibronic N and N' states involved in the absorption process are connected by total RET collision rates to two additional "lumped" states that include the whole remaining rotational manifold of the ($X, v=0$) and ($A, v=1$) vibro-electronic states. Given that RET rates, although somewhat uncertain, are very high, it was shown in [49] that the model outcomes are substantially independent of the exact values of RET rates, provided these are sufficiently larger than

the absorption rate. Then the model can be simplified by dropping the two equations for the lumped states and setting the N and N' states always at Boltzmann equilibrium with the gas temperature. This is equivalent to saying that RET are so fast that both X and A rotational manifolds achieve equilibrium with the gas temperature at any time during the laser pulse. The validity of this four-level model was empirically tested with a 250 μm diameter laser beam with energy up to 9 μJ . In the previous models the spatial distribution of the laser beam is assumed to be uniform. Only in [47] it was taken into account, with a test of different functional forms of the spatial dependence of the laser fluence.

RET collisions in both X and A states can be neglected in the linear regime, since the depletion of the initial state and its refilling by stimulated emission is negligible. In addition, to assume a spatially uniform laser beam is a good approximation. Thus in the linear regime the rationalization of the LIF process is greatly simplified, since phenomena that are difficult to model can be neglected. It is then critical to establish the laser energy range in which linearity is achieved. As a rule of thumb, with current spectral bandwidths of dye lasers, and with beam section of the order of 1 mm diameter, linearity is found up to few μJ of laser pulse energy, for the transitions of scheme 1. On the other hand in an ATP plasma jet a sub-mm space resolution is required. The laser beam section can be reduced by a focusing lens to the order of a 100 μm diameter, that is suitable for jet space scales. As a consequence, linearity is found at energies below 0.1 μJ , while the sampled volume, i.e. the LIF signal, is also reduced by about two orders of magnitude. To ensure space resolution and sensitivity it is then necessary to operate LIF in a partially saturated regime. We present in the following a detailed model that takes into account RET processes in both X and A states and a non-uniform (gaussian) space distribution of the laser fluence. The aim is to understand better the whole process and to provide a realistic description that allows to operate LIF in a partially saturated regime with a focused beam.

4.2. Five-level model

We describe the LIF process by a 5-level system, schematically represented in Figure 4, in which the time evolution of the population of five states is calculated. We choose to label as population the density of a specie, and not the number of molecules, since we want to write the sampled volume explicitly in the formulas. As in [48, 47] RET collisions are taken into account by two rate equations for “lumped” states:

$$\begin{aligned}\frac{dP_{X_N}}{dt} &= -B\mathcal{E}_L(t)\psi(P_{X_N} - P_{A_{1N}}) + (\mathcal{F}_{X_N}P_X - P_{X_N})K_{X_R} \\ \frac{dP_{X_L}}{dt} &= -(\mathcal{F}_{X_N}P_X - P_{X_N})K_{X_R} \\ \frac{dP_{A_{1N}}}{dt} &= B\mathcal{E}_L(t)\psi(P_{X_N} - P_{A_{1N}}) - Q_{A_1}P_{A_{1N}} - K_{A_R}(P_{A_{1N}} - \mathcal{F}_{A_N}P_{A_1})\end{aligned}$$

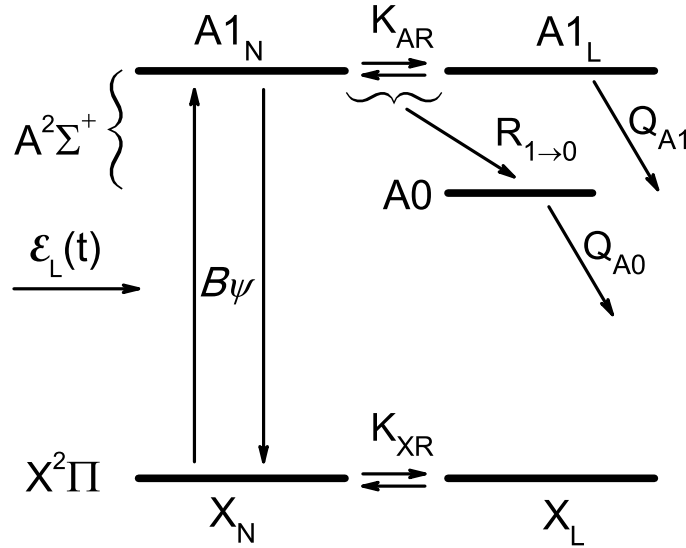


Figure 4. Scheme of the five levels of the model and of their mutual interactions. See text for symbols explanation.

$$\frac{dP_{A1L}}{dt} = K_{AR}(P_{A1N} - \mathcal{F}_{A_N}P_{A1}) - Q_{A1}P_{A1L}$$

$$\frac{dP_{A0}}{dt} = R_{(1\rightarrow0)}P_{A1} - Q_{A0}P_{A0}$$

with :

$$P_X = P_{X_N} + P_{X_L}$$

$$P_{A1} = P_{A1N} + P_{A1L} \quad (6)$$

- X_N is the (X , $v=0$, N , e or f) state that absorbs the laser photons, $A1_N$ is the (A , $v'=1$, N' , e or f) state;
- X_L is the sum of all the rotational levels of (X , $v=0$) except N . In the equation X_N is depleted by absorption of the laser light, re-populated by stimulated emission from (A , $v'=1$, N' , e or f) and by RET collisions from X_L . The refilling of X_N by RET from X_L is described by a term proportional to the difference between the actual X_N population and its equilibrium population, given by $\mathcal{F}_{X_N}P_X$, where \mathcal{F}_{X_N} is the rotational population factor (fraction) of X_N at a given temperature. This is an approximation. The correct calculation should treat individual rotational levels with state-to-state rotational energy transfer rates. Both the poor knowledge of state-to-state rate coefficients and the difficulty of such a task recommend the approximation with a single equation for a “lumped” X_L state.
- $A1_L$, analogously is the the sum of all the rotational levels of (A , $v'=1$) except N' . $A1_N$ is populated by optical absorption and depopulated by stimulated emission, spontaneous emission and by collisions with neutrals (Q_{A1} =radiative plus electronic quenching plus vibrational relaxation rate). The rotational coupling

between $A1_N$ and $A1_L$ is described in the same way as for the ground state case;

- $A0$ is the (A , $v=0$) total rotational manifold, that is populated by vibrational relaxation from (A , $v=1$) with rate $R_{(1\rightarrow0)}$ and depopulated by electronic plus radiative quenching with rate Q_{A0} ;

The initial conditions for the populations are: $P_{A0}(t=0) = P_{A1}(t=0) = 0$, $P_{X_N}(t=0) = \mathcal{F}_{X_N}[OH]$, $P_{X_L}(t=0) = [OH] - P_{X_N}$. $P_{X_N}(t=0)$ is the initial population of $OH(X, v=0, N, e \text{ or } f)$, given by the product of the rotational population factor \mathcal{F}_{X_N} and the OH density.

The optical processes are calculated as follows.

- B is the Einstein coefficient for absorption. When the statistical weights are equal for both initial and final state, as it is for Q branch transitions, $B_{X\rightarrow A} = B_{A\rightarrow X} = B$.
- $\mathcal{E}_L(t)$ is the radiant energy density of the laser, that is a function of time, given by $W(t)/cS$ with c the velocity of light, S the laser beam section and $W(t)$ the laser power. We have calculated $W(t)$ using a measured laser time profile normalized such that the time integrated $W(t)$ is equal to the measured laser pulse energy E_L .
- ψ is the spectral overlap integral. Its calculation is detailed in appendix b.

Measured quantities are the fluorescence pulse and the spectrally resolved fluorescence. They are related to model results as follows. The fluorescence pulse $S(t)$ can be measured by a photomultiplier. It is the sum of the contribution of the two bands:

$$S(t) = S_1(t) + S_0(t) = \mathcal{C}V_s(A_{(1,1)}P_{A1}(t) + A_{(0,0)}P_{A0}(t)) \quad (7)$$

$A_{(1,1)}$ and $A_{(0,0)}$ are the radiative rates of (1,1) and (0,0) bands and V_s is the sampled volume. The spectrally resolved fluorescence $\mathcal{I}_{LIF}(\lambda)$ can be measured by an ICCD with a time integration of the pulse:

$$\mathcal{I}_{LIF}(\lambda) = \Psi_{(1,1)}(\lambda) \int_0^{T_G} S_1(t)dt + \Psi_{(0,0)}(\lambda) \int_0^{T_G} S_0(t)dt \quad (8)$$

The two $\Psi(\lambda)$ are the normalized emission spectra of (1,1) and (0,0) bands. T_G , the ICCD time gate, is larger than the fluorescence lifetime. \mathcal{C} is a constant accounting for the transfer function of the optical collection plus measuring apparatus:

$$\mathcal{C} = \frac{\Omega}{4\pi} T \eta e G R \quad (9)$$

Ω is the solid angle subtended by the collection optics, i.e. by a 1 inch lens at a 200 mm focal length distance from the sample. T is the transmission factor of the fluorescence collection optical path, given by the grating efficiency at 3100 Å and by the loss of the transmitting/reflective surfaces of the path. η is the quantum efficiency of the photo-cathode, G the gain of the photomultiplier and e , the electron charge, converts the number of photoelectrons per second into a current. $R=50 \Omega$ is the input resistance of the digitizing oscilloscope. The quantitative analysis of LIF

outcomes then requires a knowledge of \mathcal{C} , of the sampled volume V_s , of the collision rates and, finally, the correct absorption rate that depends also on the laser beam section. Although \mathcal{C} can be determined by a calibration of the optical arrangement, V_s is a critical parameter especially with a focused laser beam, due to the fact that the laser energy is not distributed uniformly in the beam section. Such a parameter requires a specific treatment, that will be addressed in the next paragraph, and must be determined by investigation of the laser energy dependence in a calibration cell.

4.3. Spatial energy distribution of the laser beam

The laser beam irradiance is not uniform in the beam section. In the frame of combustion research, in order to get rid of the collision quenching in unknown gas mixtures, the so called saturated fluorescence spectroscopy was proposed (see [47] and references therein), since running LIF in high saturation conditions makes the LIF outcome independent of electronic quenching. Unfortunately true saturation is very difficult to achieve due to the spatial non-uniformity of the beam. Calculations with a 2D gaussian energy distribution:

$$E_{las}(r) \propto \exp(-r^2/w_0^2) \quad (10)$$

were proposed in [50], showing a logarithmic dependence of the LIF outcome on the laser energy. In [47] the effect of top-hat, triangular, lorentzian and gaussian profiles were tested. In our case, the use of a spatial filter to clean the laser beam can give out an almost gaussian beam distribution. This should be verified experimentally. We have not actually the possibility to perform such a test, then we use a gaussian distribution as a reasonable assumption for pointing out the effects of a spatial distribution. The treatment of this issue in the model calculations is detailed in appendix c.

4.3.1. Good practice notes. The spatial profile of the laser beam that reaches the sampled volume is the result of many passages through optical elements for beam positioning, attenuation and focusing, in addition to optical windows at the discharge entrance. Although the far field laser profile might be near gaussian, multiple reflections and diffusion from optical surfaces can add diffused baffles to the borders of the beam. To work with a clean laser spot, a spatial filter at the last stage of the beam handling optics is advisable. We have used a filter composed of a couple of 100 mm fl lenses set 200 mm apart each other, with a 50 μm pinhole in the middle of the arrangement. The spatial filter removes the spurious baffles as well as the multiple-order energy peaks of the beam diffraction pattern. The assumption of a gaussian beam profile has not been verified experimentally, and we cannot exclude deviations from it. We only point out that the saturation characteristics are quite well reproduced by assuming a gaussian profile (see section 5). A good practice should include a measurement of the beam spatial profile in the sampled volume.

Table 1. Rate coefficients for $OH(A^2\Sigma^+, v = 0, 1)$ total collision quenching (Q + VET) and $1 \rightarrow 0$ vibrational relaxation at T=300 K by He, Ar, N₂, O₂ and H₂O ($10^{-11} \text{cm}^3 \text{s}^{-1}$). Radiative rates are also reported (from [4]).

	v=0	v=1	$1 \rightarrow 0$	ref.
He		0.004 ± 0.0015^a	0.002^a	[17]
			0.13 ± 0.04	[51]
Ar	$\leq 0.03^a$	0.3^a	0.27^a	[17]
			0.41 ± 0.03	[52]
			0.32 ± 0.04	[51]
N ₂	2.8 ± 1.2^a	23.6 ± 1.5^a	23.3 ± 2.2^a	[52]
	2.7 ± 1.0			[53]
		24.1 ± 1.3	21.1 ± 2.1	[54]
		19 ± 1.5	24 ± 3	[55]
			14	[56]
H ₂ O	68.0 ± 6.1^a			[57]
	69.1 ± 5.0			[58]
		66 ± 4^a	≤ 12	[55]
			7.3 ± 0.5^a	[52]
O ₂	9.6 ± 1.2	20.6 ± 1.5	2.1 ± 0.2	[52]
	9.2 ± 1.5			[53]
		20.2 ± 1.6	3.3 ± 0.7	[54]
		17	1.5	[56]
rad.	(s^{-1})	(s^{-1})		
A_{tot}	1.458×10^7	1.329×10^7		[59]
$A_{(0,0)}$	1.451×10^7			LIFBASE database
$A_{(1,1)}$		8.678×10^6		LIFBASE database

^a Value recommended in [17]

4.4. Collision data

Total quenching rates of level (A,v=0), Q_{A0} , level (A,v=1), Q_{A1} , and the VET rate from v=1 to v=0, $R_{(1 \rightarrow 0)}$ can be calculated with good accuracy in He/Ar + H₂O + air since rate coefficients for these gases are well known. The data are reported in tab. 1.

RET rates in the A state are dependent on the rotational level and on the collider molecule, and have been investigated mainly for (A,v=0). Calculations for N=1-5 are reported in [60], that agree quite well with the measurements of [61]. For (A,v=1) measurements exist only for F₁(4) F₂(5) with various colliders [62]. In that paper it was observed that RET rate coefficients are very similar in magnitude to those of (A,v=0). We then use for our calculations the theoretical values reported in [60]. In the conditions of the calibration cell and of the jet used for the saturation curve, the dominant RET contribution is from He collisions. Total RET rate coefficients for collision with He are $2.01 \times 10^{-10} \text{cm}^3 \text{s}^{-1}$ for F₁(1) and $1.37 \times 10^{-10} \text{cm}^3 \text{s}^{-1}$ for F₁(2). Then, for Q₁(1) line

$K_{A_R} = 4.9 \times 10^9 s^{-1}$, and for $P_1(3)$ line $K_{A_R} = 3.3 \times 10^9 s^{-1}$. RET rate coefficients in the ground state are not well known, but are thought to be slightly larger than those of the A state [63]. In [64] and references therein, the recovery rate of an initially depleted level of the X state was measured in various combustion mixtures at high temperature. For low N level rates of the order of $(3-6) \times 10^9 s^{-1}$ were found, almost independent of the gas mixture. We have chosen to use $K_{X_R} = 4 \times 10^9 s^{-1}$. Note that we have verified that K_{X_R} and K_{A_R} values larger than about $2 \times 10^9 s^{-1}$ do not modify appreciably the results of the model calculations. The addition of molecular gases generally increases RET rates, so that this choice of RET rates can be applied also to cases with a significant presence of molecular gases.

4.4.1. Other molecules. The knowledge of collision rate constants for other molecules of interest in ATP discharges research is not as well detailed as for OH. Again much of this knowledge comes from combustion research. RET processes have been studied in $N_2(B^3\Pi_g)$ [65], $NO(A^2\Sigma^+)$ [66], $CH(A^2\Delta)$ [67], $CH(B^2\Sigma^-)$ [68, 69], for various colliders. VET studies can be found in [70, 71, 69] for $CH(A^2\Delta, B^2\Sigma^-, v = 1)$, in [72] for the whole $N_2(C^3\Pi_u, v = 0 - 4)$ vibrational manifold. Electronic quenching of $NO(A^2\Sigma^+)$ and $CH(A^2\Delta)$ states has been deeply investigated, and a discussion on the quenching cross sections and rate coefficients by many colliders in the wide temperature range 300-2500 K can be found in [73].

5. Quantitative analysis

5.1. Saturation characteristics and calibration constant

Absolute LIF measurements require a calibration that is basically needed for the determination of the CV_s product. Many methods have been proposed, a survey of which can be found in [4]. In ATP plasma jets we have two examples in the literature. In [20] the calibration constant was determined by Rayleigh scattering on air molecules in open air. In [42] a DBD discharge was placed in the same position as the plasma jet and used as a source of OH, whose concentration had been previously determined by TR-BBAS. In [49] various OH calibration methods are compared. Although tested in a nanosecond pulsed plasma filament, these methods are useful for plasma jets too, and indeed for any ATP discharge type. Rayleigh scattering, broadband absorption on the tiny plasma filament and a chemical model in the afterglow were compared in that paper.

Here we have used a calibration cell as in [42]. The calibration has been performed for the two laser conditions with and without focusing lens. Measurements have been taken in the conditions of fig. 7 of [34], i.e in a discharge with $[H_2O] = 0.56\%$ (concentration fraction), 4.5 mm inter-electrodes gap and six different values of discharge power. Laser pulse energy of about $5.3 \mu J$ (not focused) and $0.4 \mu J$ (focused) have been used with $Q_1(1)$ line excitation. The LIF outcomes have been compared to the

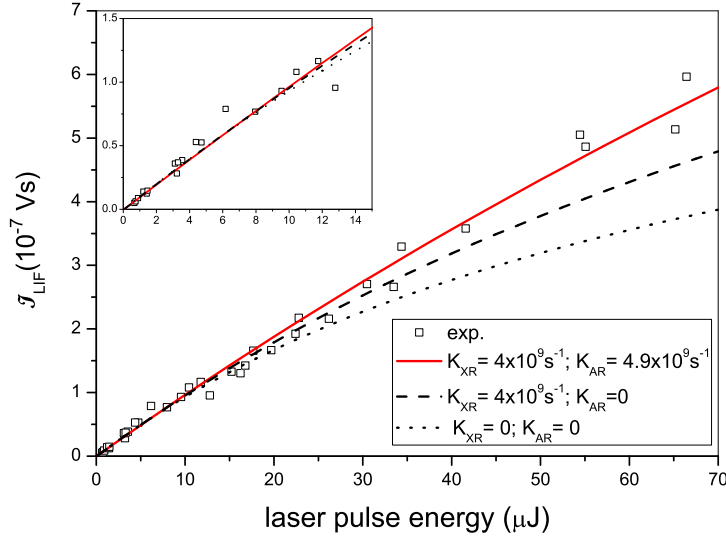


Figure 5. \mathcal{I}_{LIF} versus laser pulse energy - unfocused beam, $Q_1(1)$ excitation. $He + [H_2O] = 0.23\%$, discharge power density of 10 W cm^{-3} . The red curve is calculated with full account of RET in the ground and A1 states. To show how RET affect the saturation curve, calculations without RET in the A1 state and without RET at all are also shown.

OH densities measured in [34] to get the value of the product $\mathcal{C}V_s$.

The methodology of a calibrated LIF measurement is based on the measurement in a well characterized condition and on the extrapolation of the calibration to a range of different conditions. Such an extrapolation requires the LIF model description to be robust with respect to the change of parameters - collision processes, laser beam energy, gas temperature - that can affect the LIF outcome. The model must then be tested by comparing its outcomes to saturation curves, i.e. LIF signal vs. laser pulse energy.

In the unfocused case shown in Figure 5, calculations with full account of RET collisions show a reasonable agreement with experiments for a beam waist $w_0 = 750 \mu\text{m}$. In the same figure, the effect of partial or total elimination of RET from the model is also shown. We can define as “linear” regime the condition in which model calculations are independent of RET collisions, i.e. in which calculations with $K_{XR} = K_{AR} = 0$ are almost equal to those with any RET rate. In other words in the linear regime the fraction of population pumped to the excited state is so low that any refill process is negligible. Such a linear regime is achieved up to, roughly, $8 \mu\text{J}$ per pulse.

Both the treatment of RET collisions and the spatial pattern of the beam are approximated. With our choice of RET treatment, the $w_0 = 750 \mu\text{m}$ value gives a good agreement with experiments as it is shown in Figure 6, where calculations with other w_0 values are presented. On the other hand, setting to zero the RET rates, a good agreement with the experimental data can still be achieved by increasing the beam size, as it is shown in Figure 7. This is however achieved at a non realistic w_0 value of 2 mm.

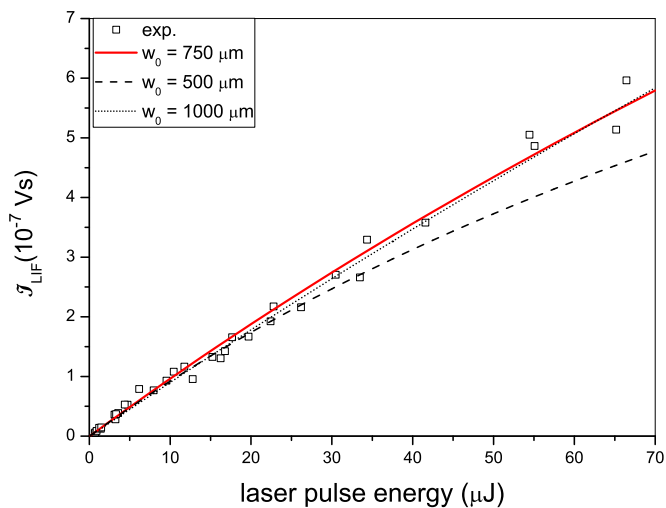


Figure 6. \mathcal{I}_{LIF} versus laser pulse energy - unfocused beam, $Q_1(1)$ excitation. $He + [H_2O] = 0.23\%$, discharge power density of 10 W cm^{-3} . Influence of the w_0 value on the saturation curve.

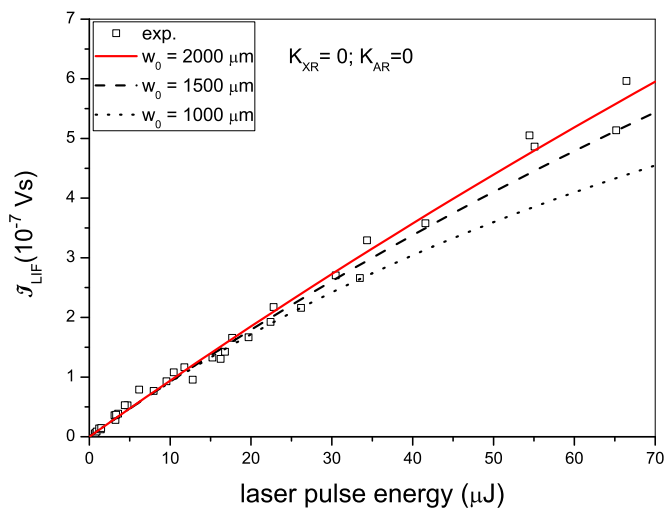


Figure 7. \mathcal{I}_{LIF} versus laser pulse energy - unfocused beam, $Q_1(1)$ excitation. $He + [H_2O] = 0.23\%$, discharge power density of 10 W cm^{-3} . Saturation curves calculated with RET rates set to zero. A good agreement is achieved at $w_0 = 2 \text{ mm}$ (red curve).

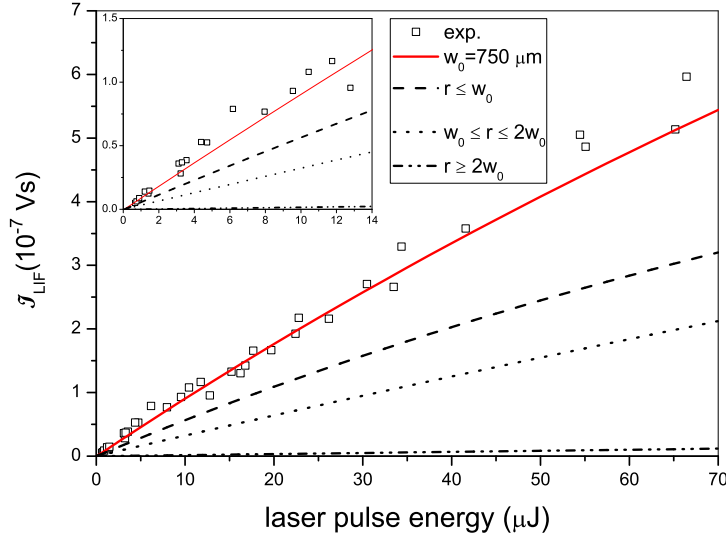


Figure 8. \mathcal{I}_{LIF} versus laser pulse energy - unfocused beam, $Q_1(1)$ excitation. $He + [H_2O] = 0.23\%$, discharge power density of 10 W cm^{-3} . Contribution of the central, intermediate and peripheric laser beam regions.

We then conclude that both spatial non-uniformity and RET collisions must be taken into account, and that reasonable values of the parameters must agree with the 2 mm diameter experimentally estimated beam size .

Finally we show in Figure 8 the contribution of the central, intermediate and peripheric space regions (see figure) to the signal. Most of the LIF signal comes from $r < 2w_0$, while, as expected, non linearity is concentrated in the $r < w_0$ circle.

In the focused beam case all these characteristic are much more evident. The smaller beam section implies about two orders of magnitude larger radiant energy densities, so that the linear regime is achieved at energies lower than $0.1 \mu J$. Working at these low energies is disadvantageous, since then the LIF signal is very low due to the corresponding two orders of magnitude smaller sampled volume. To deal with sufficient signal, then, we must operate the experiment in a partially saturated regime, where all the RET and spatial effects are very important. The saturation curve in the calibration cell is shown in Figure 9, together with model calculations with $w_0 = 80 \mu m$ and the same RET rates as in the unfocused case.

A good agreement is observed up to $15 \mu J$. Note also that the first part of the curve might even be fitted by a linear function, showing that saturation curves in a limited energy range can be erroneously interpreted as a linear regime with a small offset (y axis intercept) due to an unidentified background in the LIF outcome, or an offset in the pulse energy measurement system. The deviation from model calculations at high energies may be due to the presence of very low energy spatial “wings” of the laser beam. These might be caused by reflections of the laser beam by the inner surfaces

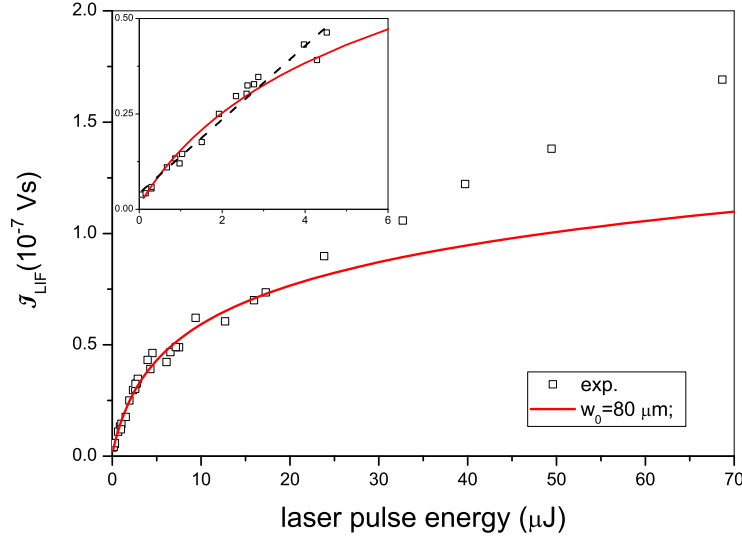


Figure 9. \mathcal{I}_{LIF} versus laser pulse energy - focused beam, $Q_1(1)$ excitation. $He + [H_2O] = 0.23\%$, discharge power density of 10 W cm^{-3} . The red curve is the model calculation with $w_0 = 80 \mu m$, $K_{X_R} = 3 \times 10^9 s^{-1}$, $K_{A_R} = 1.2 \times 10^9 s^{-1}$. In the inset figure the dashed line is a linear fit of the low energy part of the saturation curve.

of the optical windows. In order to exclude such an occurrence, we have measured the saturation curve also in the plasma jet, where the absence of windows on the laser path and the small volume of the active plasma region exclude this possibility. No difference has been observed between saturation curves in the reference cell and in the plasma jet. Such a spurious effect can then be excluded. Another possibility is that, tuning on the $Q_1(1)$ line, spectral wings of the laser line can be absorbed by the adjacent $Q_{12}(1)$. We have then measured the saturation curve also on the isolated $P_1(3)$ line. Note that the two lines have similar absorption coefficients, namely 1.772 and $1.604 \times 10^{17} m^3 J^{-1} s^{-2}$, respectively. A small difference between the two cases shows the presence of a small linear contribution due to absorption by the $Q_{12}(1)$ line. We have then tested the model on the $P_1(3)$ saturation curve.

Figure 10 shows results of model calculations with full RET account. A good agreement is achieved for $w_0 = 80 \mu m$. As in the unfocused case we show the effect of RET collisions in Figure 11, and, in Figure 12, how an agreement can be reached without the RET collisions with larger, non realistic w_0 values. The choice of $w_0 = 80 \mu m$ is then made since such a value is closer to the calculated waist. In practice, in the focused case we use the $P_1(3)$ saturation curve in the jet to fix a reasonable value of w_0 and then the $Q_1(1)$ measurements in the calibration cell to get the calibration constant.

Finally, with $K_{X_R} = 4 \times 10^9 s^{-1}$, $K_{A_R} = 4.9 \times 10^9 s^{-1}$, we get:

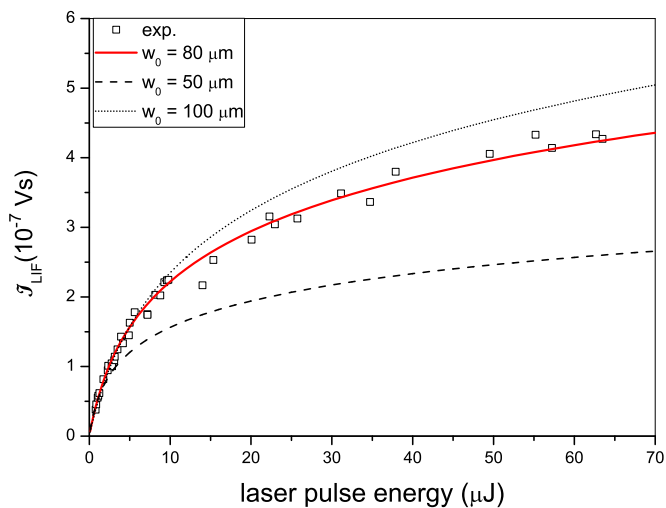


Figure 10. \mathcal{I}_{LIF} versus laser pulse energy - focused beam, $P_1(3)$ excitation. He plasma jet with 3.1 Torr H_2O and 3.2 Torr of air. Calculations are made with three values of w_0

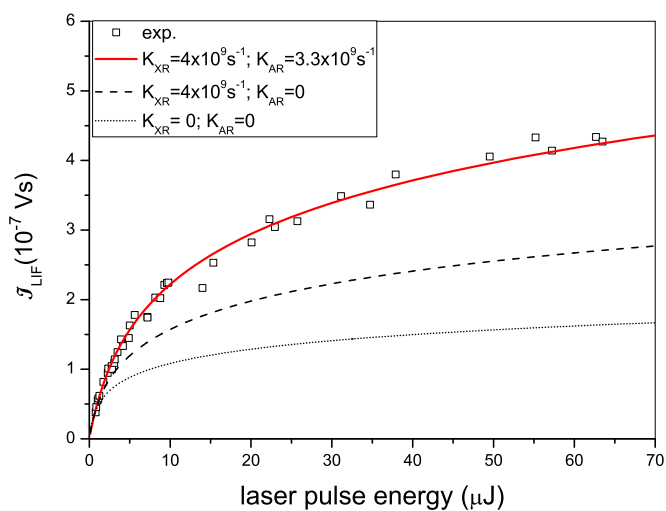


Figure 11. \mathcal{I}_{LIF} versus laser pulse energy - focused beam, $P_1(3)$ excitation. He plasma jet with 3.1 Torr H_2O and 3.2 Torr of air. The red curve is calculated with full account of RET in the ground and A1 states. To show the effect RET on the saturation curve, calculations without RET in the A1 state and without RET at all are also shown.

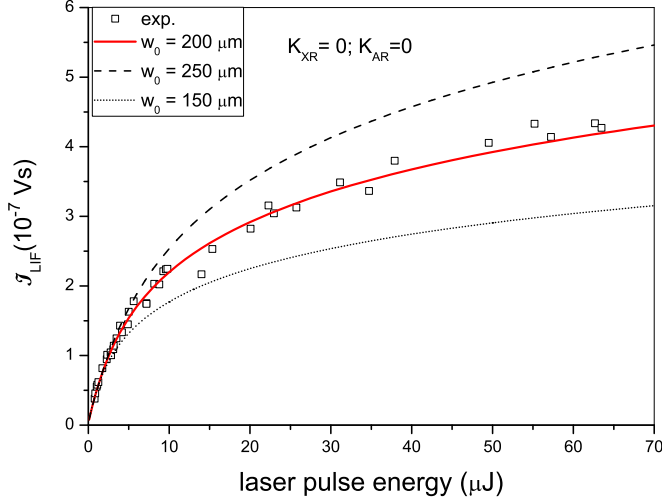


Figure 12. \mathcal{I}_{LIF} versus laser pulse energy - focused beam, $P_1(3)$ excitation. He plasma jet with 3.1 Torr H_2O and 3.2 Torr of air. Saturation curves calculated with RET rates set to zero. A good agreement is achieved at $w_0 = 200\mu m$ (red curve).

$$\begin{aligned} \mathcal{C}\tilde{V}_s &= (7.00 \pm 2.12) \times 10^{-18} \text{ V cm}^3 \text{ s} & w_0 &= 750\mu m & \text{unfocused} \\ \mathcal{C}\tilde{V}_s &= (1.54 \pm 4.32) \times 10^{-19} \text{ V cm}^3 \text{ s} & w_0 &= 80\mu m & \text{focused} \end{aligned} \quad (11)$$

where \tilde{V}_s has here the meaning of an “effective” volume.

For the focused case also we show in Figure 13 the contribution of the central, intermediate and peripheric space regions (see figure) to the signal. At energies roughly below $1\mu J$ the contribution of the peripheric region is negligible, and the spatial resolution is within $2w_0$. At higher energy the increase of LIF signal is obtained also at the expense of a lower spatial resolution.

5.1.1. Good practice notes A good saturation characteristic with focused beam can be retrieved provided low pulse energies can be handled and measured. In our apparatus we started with low energy by excluding the dye amplifier, then working only with the oscillator and pre-amplifier. The energy is then reduced by means of a self-made attenuator, based on the design of [74]. It is composed of two counter-rotating couples of UVFS beam splitters, and performs a maximum attenuation of 34 dB.

The measurement of the laser energy is made by two energy meters, for low and high pulse energy. The low pulse energy meter is a silicon-based thermopile (DX-0576, Dexter research center). It is used for energy lower than $4\mu J/\text{pulse}$. The sensor has an active area of 2.25 mm^2 and a typical responsivity of 31 V/W , an equivalent series resistance of $R_s = 90\text{ k}$ and a time constant of $\tau_s = 38\text{ ms}$. The signal is amplified

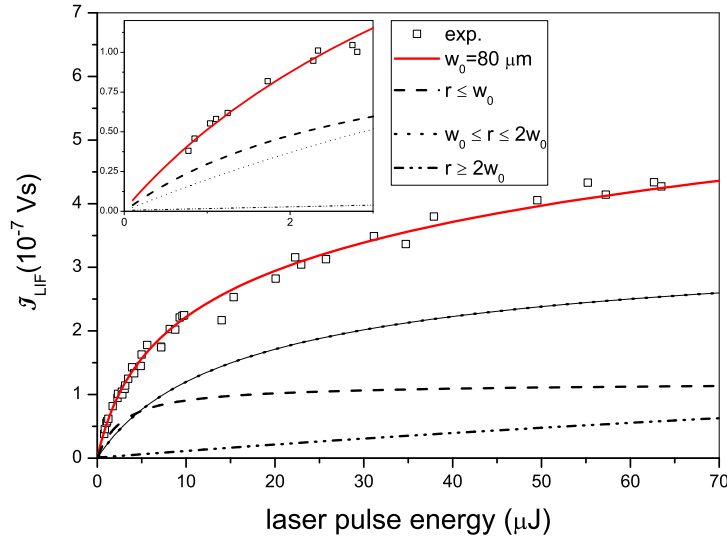


Figure 13. \mathcal{I}_{LIF} versus laser pulse energy - focused beam. $P_1(3)$ line, He plasma jet with 3.1 Torr H_2O and 3.2 Torr of air. Contribution of the central, intermediate and peripheral laser beam regions.

by a factor of 500 by a non-inverting, low-noise amplifier. The high energy meter is a pyroelectric detector (P1-13 Molectron) followed by an amplifier with a factor of 10 gain.

5.2. Gas mixture composition

LIF is a suitable diagnostic technique for strongly inhomogeneous media, like Plasma Assisted Combustion or Plasma Jet systems. One such inhomogeneity is in the local gas mixture composition. The local collision rates involved in equations 6 must be known. These can be obtained by measuring simultaneously the fluorescence pulse $S(t)$, the decay of which is a measure of the total electronic quenching rate, and the fluorescence spectrum $\mathcal{I}_{LIF}(\lambda)$, in particular the ratio of the two fluorescence bands, from which the vibrational relaxation rate can be inferred. This is sufficient for quantitative LIF measurements, without the need of a detailed knowledge of the gas mixture composition. If rate coefficients are well known, however, it is possible to infer the gas composition using the collisional data measured by LIF. In [21] for a plasma jet expanding into free air the total electronic quenching was measured from the LIF pulse decay, and the concentration of humid air penetrating into the jet was calculated for a fixed air plus water vapour mixture. A plasma jet expanding into ambient humid air and hitting a liquid surface, instead, has not a fixed humid air composition. In addition, residual humidity in the feeding gas and jet tubes can add uncertainty to the mixture. Air and H_2O partial pressures must be determined independently. Since the collision rate constants are well known (see tab. 1), the gas composition can be measured,

and then accounted for in the LIF outcome, on the basis of the collision quenching and vibrational relaxation. It was demonstrated in [75] that a unique He + air + H₂O mixture composition corresponds to a given couple of electronic quenching and vibrational relaxation rates values. Here we implement this idea by measuring at each spatial position both $S(t)$ and $\mathcal{I}_{LIF}(\lambda)$ and fitting them by the model 6 using the concentrations of air and water vapour as parameters. The electronic quenching is given by the decay of $S(t)$, while the ratio of the integrated emissions from the two bands depends on the VET rate. Examples of measured and simulated $S(t)$ and $\mathcal{I}_{LIF}(\lambda)$ in a jet at different positions cases are shown in the figure 3 of [42]. Such method has been applied for the first time in [42] to a pulsed HV Plasma Jet (Plasma Gun) hitting a humid surface.

5.2.1. Good practice notes. $S(t)$ and $\mathcal{I}_{LIF}(\lambda)$ must be measured sequentially. In our apparatus the PMT and ICCD are mounted on the two exit ports of the monochromator. The switch from one exit port to the other is obtained by a motorized mirror inside the monochromator that can be operated under computer control. We point out that sampling the same spatial region for the two measurements is of fundamental importance. The idea of measuring simultaneously $S(t)$ and $\mathcal{I}_{LIF}(\lambda)$ by two monochromators and a beam splitter before the entrance of the two is not feasible, since sampling the same volume by the two would require a perfect alignment. The only possibility for a simultaneous measurement would be to replace the switching mirror with a beam splitter inside the monochromator: for trained personnel only!

5.3. Gas temperature measurement

The gas temperature is an important parameter to be taken into account to rationalize LIF outcomes. It determines both the initial population of the absorbing rotational state and the linewidth, which in turn affects the overlap integral ψ . In discharges that do not develop a high gas temperature, say less than 400 K, like the pulsed DBD of our calibration cell, or the pulsed plasma gun in [42], a space resolved measurement of the local temperature is not strictly necessary if the laser excitation scheme involves low N levels since the population, as well as the overlap integral, do not change appreciably. On the contrary, cases in which the gas temperature is higher, like a RF plasma jet, require a local measurement of the gas temperature. The safest way to measure the rotational temperature of OH(X,v=0) is to fit the LIF excitation spectrum by a synthetic spectrum, like in [76] or in [27]. This kind of measurement usually involves largely spaced rotational lines, and is then quite time consuming and/or affected by a large error. In order to get a better accuracy in a shorter time, and thanks to the quite narrow bandwidth of our laser, we choose to measure excitation spectra that, in a short spectral interval, include the closely spaced Q₁₂(1), Q₂(1), Q₁(6), Q₁₂(3) and Q₂(3) lines. One such spectrum, taken in the conditions of the calibration cell, is shown in Figure 14. This methodology allows a good accuracy. From the spectrum of Figure 14 a ± 10 K error can be estimated.

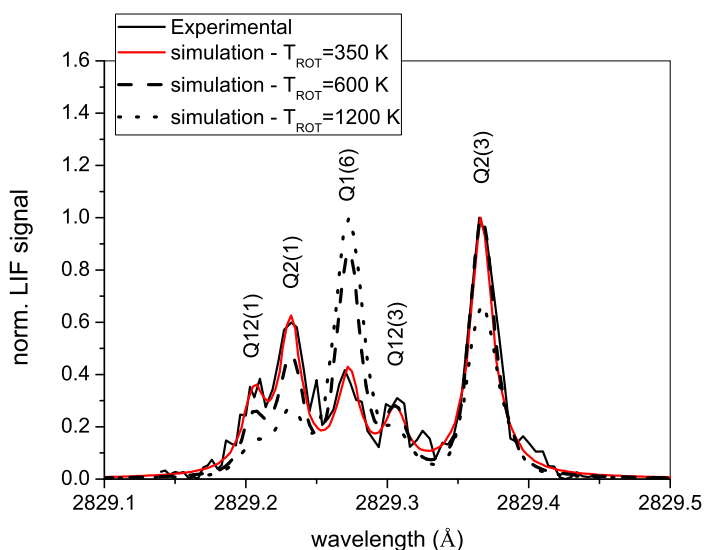


Figure 14. LIF excitation spectrum and model simulation for the measurement of the gas/rotational temperature. Simulated spectra at high temperature are also plotted to show how the spectrum changes on rising significantly the temperature.

The sensitivity at higher temperatures remains large, as it is shown in Figure 15 where the peak intensity ratios are shown as a function of temperature up to 1200 K. The time required for completing the wavelength scan is about 7 min.

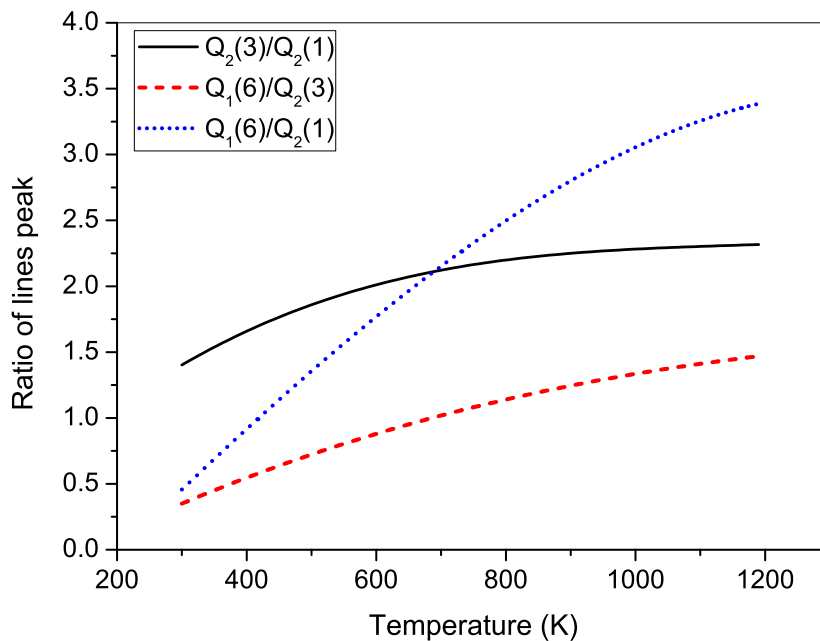


Figure 15. Ratio of the main lines peak intensity in the spectrum used for temperature measurements. The ratios are calculated from LIFBASE spectra simulations.

The correct measurement of excitation spectra would require to work rigorously

within the linear regime. In our case we can work also in partially saturated regime. A correction, taking into account the differences in the absorption coefficients of the various transitions, is possible using the saturation characteristic. The LIF signal in fact depends on the product of absorption coefficient and laser energy, so that an absorption coefficient change is equivalent to a laser energy variation. Nevertheless, looking at the absorption coefficients in tab. 2, we observe that the most important lines, $Q_2(1)$, $Q_1(6)$ and $Q_2(3)$, have similar absorption coefficients, so that working in a weak saturation regime does not imply large temperature errors. The fitting temperature of the spectrum in Figure 14 in fact coincides with that measured by TR-BBAS in the calibration cell. On the other hand the remaining lines, $Q_{12}(1)$ and $Q_{12}(3)$, have much lower absorption coefficients, so that in saturation regimes their relative intensity will be overestimated.

Table 2. wavelengths and absorption coefficients of the lines used for temperature measurements (from LIFBASE database)

line	wavelength (\AA)	abs. coeff. ($m^3 J^{-1} s^{-2}$)
$Q_{12}(1)$	2829.21	1.051×10^{17}
$Q_2(1)$	2829.23	2.102×10^{17}
$Q_1(6)$	2829.27	2.852×10^{17}
$Q_{12}(3)$	2829.31	5.441×10^{17}
$Q_2(3)$	2829.37	2.390×10^{17}

It is worth mentioning at this point that a simpler method is available for the temperature measurement in gas mixtures with prevailing noble gas component, as it is the case in the core of He plasma jets expanding into humid air. Provided the RET rate is much larger than the quenching rate of OH(A) state, rotational equilibrium to the gas temperature is achieved in the fluorescence spectra. This ratio, that is the number of RET collisions in the lifetime of the electronic state, is reported in Figure 16. It can be seen that at least up to 10 Torr of air, the number of RET collisions is sufficient for the thermalization of the A state rotational distribution. In the jet periphery, then, where the lifetime is short, the temperature can no longer be deduced from fluorescence spectra.

5.3.1. Good practice notes. Since the time spent for a temperature measurement by an excitation spectrum can be quite long, it is worth to try to shorten it. Much of the time for a spectrum recovery is due to the tuning of the laser that is achieved by moving the grating of the oscillator cavity by means of a stepping motor. We have implemented a faster scanning mechanics, in which short displacements of the translation stage that moves the laser tuning mirror are achieved by a piezoelectric actuator. The actuator maximum displacement is $12 \mu m$, allowing a wavelength range of 1.6\AA , that is more than enough to cover the entire spectrum of Figure 14. The piezo movement is almost instantaneous. In this way dead times of the stepping motor movement are eliminated, and the repeatability of the wavelength scan is improved.

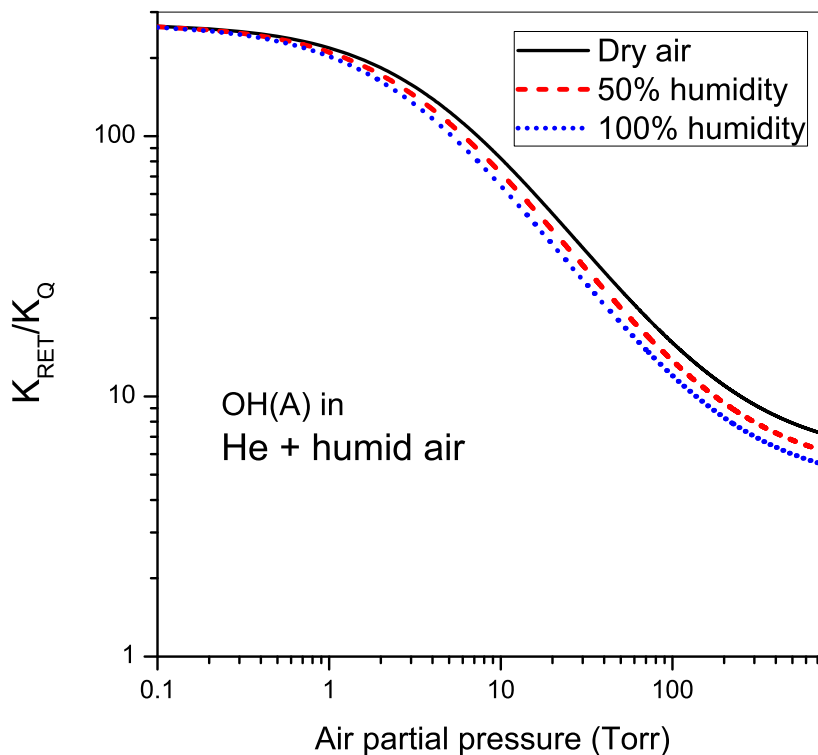


Figure 16. Ratio of RET over quenching collision rate as a function of air partial pressure in He buffer gas.

The spectrum for temperature measurements is made of less intense lines than the low N of Q_1 and P_1 branches, since the low N lines all belong to the F_2 sublevel, that has a smaller population. Nevertheless the spectrum itself can be used for absolute OH concentration measurements, especially in the unfocused case, where abundant signal is available, performing in this way a simultaneous measurement of both the OH concentration and the temperature. On the other hand, when measuring LIF signal on a fixed line, drifts of the laser wavelength must be avoided with stabilization or feedback systems. In order to circumvent slow detuning in long lasting experiments, it is anyway a good practice, also on a single line, to measure each time the excitation spectrum, in which each point of the spectrum contributes to the statistics of the whole measurement. We have used this methodology for the measurements in the jet we are going to describe in the following section.

6. Measurements in the RF jet

We report here one measurement in the RF plasma jet as an example of application of the technique. The jet flow impinges over the surface of a commercial mixture of oilseeds, and some water is added into the main He flow in order to increase the OH density and flux over the oil surface. The experiment is aimed at studying the oxidation of lipids and on the eventual role of OH in this process. The concentration of OH, air

and water, and the rotational temperature, are reported in Figure 17. For the sake of readability, the experimental points are interpolated in the maps.

The plasma jet is in fact a discharge, with capacitive coupling of the RF electrode with the grounded electrode below the oil vessel. The discharge path follows the fluid dynamic path of the He mainstream. The OH map shows quite clearly a deviation towards the right side of the flow, that was also visible by naked eyes. From the air map it appears that this deviation is due to an asymmetry of the co-flow that allows more air to penetrate from the left side. Such an air penetration into the left side of the discharge region could be the reason for the temperature increase in the same side. It is not our aim here to discuss into detail the discharge and flow dynamics of the jet + target system. We just want to underline the importance of local, independent measurements of the gas components and temperature in this kind of systems. We finally observe that the spatial resolution of the measurements is of the order of 0.2 mm, so that we are still averaging over a space scale comparable to that of concentration and temperature gradients.

6.0.2. Good practice notes. The plasma induced emission (PIE) of the OH 3064 Å system from the discharge is very intense. This is one of the reasons why it is advisable to operate LIF with a sufficiently large signal as to overcome the PIE. The LIF pulse $S(t)$ can be separated temporally from PIE, with a baseline subtraction. $\mathcal{I}_{LIF}(\lambda)$ requires instead a double measurement, with and without laser, to separate LIF from PIE. In addition, especially in RF jets, the continuous, intense PIE can easily create a condition of photomultiplier voltage divider saturation. This kind of saturation is achieved at much lower light levels than pulse saturation, forcing to attenuate the light reaching the PMT down to levels much lower than those allowed by pulsed operation. The way out of this is operation of LIF in the post-discharge of a pulsed discharge, at post-discharge times such that PIE has dropped while OH concentration remains almost constant due to its slow kinetics compared to that of the excited state. This is easily done in dielectric barrier discharges with sinusoidal or pulsed excitation [17] or in jets with pulsed excitation [42]. We have operated the RF excitation in such a way as to switch it off for 10 ms at the 10 Hz laser repetition rate, and synchronized the laser pulse to the RF modulation with a 14.6 μs delay after switch-off. Since the discharge is switched-on most of the time, the PMT is still under voltage divider saturation. Use of a gated PMT is then mandatory. Although nowadays gated PMTs can be found on the market at affordable prices, we have used a home made voltage divider circuitry for our classical PMT. Our PMT is a 12-stage end window linear type. High voltage, fast IGBTs are used to invert the polarity of the voltage bias between dynodes 5 and 6 and dynodes 6 and 7, thus stopping the transit of electrons, on application of a TTL gating signal. An attenuation larger than 5×10^5 is obtained when the gate signal is low, with a switch-ON time (time to reach steady state signal amplification) of 1.25 μs .

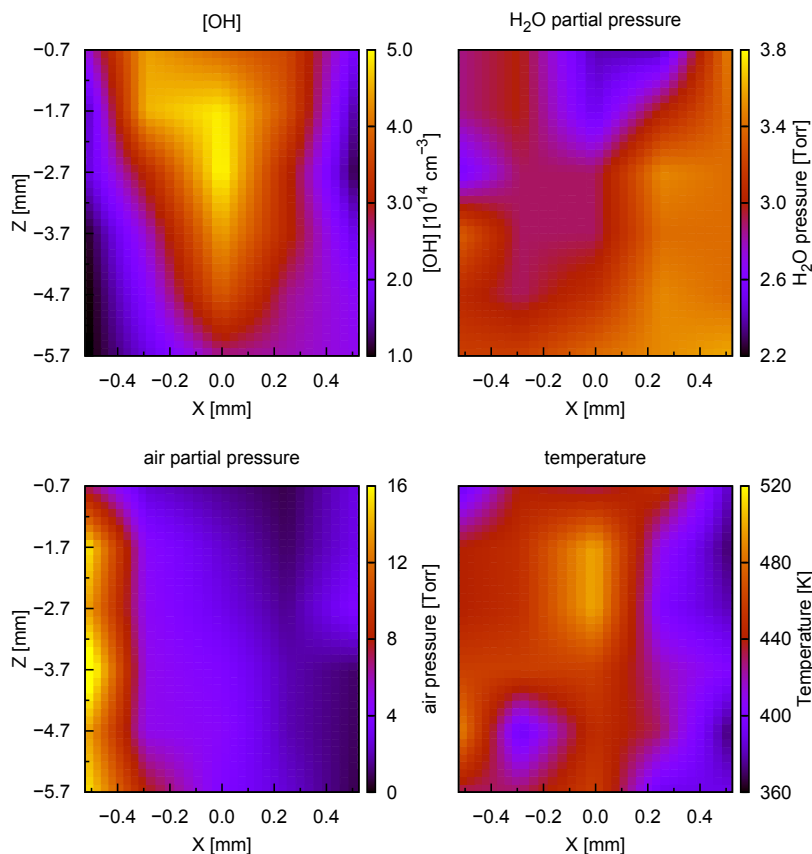


Figure 17. Maps of OH, air and water concentration, and rotational OH temperature in the effluent jet impinging on an oilseed target. Z is the distance from the jet edge. The target is at -6.2 mm from the edge. The maps are made of 30 interpolated experimental points. The effluent flux is a 2000 sccm He + 0.45% H_2O mixture, with a 2000 sccm of He co-flow. RF power = 2.7 W.

7. Conclusions

This paper explores quantitative LIF measurements of molecular radicals at atmospheric pressure, through its application to the OH radical. The rationalization of the experimental outcomes requires a rate equation model that must take into account:

the collision processes. Electronic quenching (Q), VET and RET processes must be known. Q and VET rates can be locally determined from LIF outcomes and used in the model. If a quantitative relationship between Q, VET rates and the gas mixture can be established through the detailed knowledge of individual rate coefficients of the gas components, then the gas composition can be measured by LIF. RET rates are not generally accurately known. Values of the order of 10^9s^{-1} are reasonably expected. Variations of RET rates above these values do not result in appreciable variations of the model outcome, unless under very high laser irradiance conditions;

the spatial non uniformity of the laser beam fluence. A gaussian beam appears to

be a reasonable approximation, especially after beam clean-up by a spatial filter. An empirical beam waist value can be found by modelling the saturation curve up to pulse energies as high as to make the tails of the gaussian beam contribute to the total LIF signal.

A calibration procedure is mandatory. Two kinds of calibration are possible. One is to apply LIF to a source of known radical concentration. The other one is to measure the product CV_s by another scattering experiment, like Rayleigh scattering. The calibration procedure must include the accurate measurement of the saturation curve, in order to infer the beam size and to choose correctly the working regime. In particular, the beam size affects the calculated laser irradiance, that is the parameter with the largest effect on model outcomes [49].

The choice of the working regime is dictated by the experimental conditions. Whenever the spatial resolution is not a concern, i.e. when typical beam diameters of the order of 1 mm are considerably smaller than the space scale of discharge gradients, the linear regime is highly desirable: RET can be neglected and a top-hat beam spatial distribution can efficiently substitute the gaussian one, since in every annulus the interaction is linear and the error in the sampled volume and irradiance can be absorbed into the calibration constant. On the contrary, when high spatial resolution is required (as it is the case in ATP plasma-jets), the choice of a moderate saturation regime is advisable for sensitivity reasons. More detailed modelling and knowledge of the laser beam characteristics are then necessary. In this condition the 5-level model with a gaussian beam is robust with respect to parameter variations. Moderate saturation ensures in addition the validity of the rate equation approach.

8. Acknowledgements

This work has been supported by the project ENAM of Provincia Autonoma di Trento in cooperation with IMCB of CNR (Italy), and by the project PON03PE-00067-6 “Apulia Space” of the Italian Ministry of Education, University and Research.

9. Appendices

9.1. Appendix a: validity of the rate equations model

The exact description of the interaction of matter with intense, coherent light is given by a density matrix formulation, the so-called optical Bloch equations [77]. In a two-level interaction with a classical electromagnetic field, the off-diagonal matrix elements contain the dipole interaction term and account for coherent effects. In the absence of any damping term, the equations have an oscillating solution at the Rabi frequency. Damping terms in the equations of the off diagonal equations are added empirically and account for processes that destroy the coherence of the interaction. Radiative decay and collision processes then have the effect of damping the Rabi oscillations up to reaching a steady-state in a time that depends on the damping rate. The validity of rate equations

(RE) in place of density matrix equations (DME) in the case of a pulsed laser field was examined in [78], where it was shown that DME formalism is equivalent to RE in the steady-state approximation, i.e. when coherence damping suppresses Rabi oscillations. In the pulsed case this condition is obtained when the damping rate is much larger than the rate of change of the electric field, or, in other words, the damping characteristic time is much less than the laser pulse rise time, so that steady state is achieved with good approximation at any time during the laser pulse. In our case, as in ordinary pulsed dye lasers, the pulse duration is about 10 ns FWHM, and the rise time is of the order of some ns. All kinds of collisions in addition to pressure broadening ones, are de-phasing events, i.e. also velocity changing collisions and quenching collisions. A pressure broadening of the order of 2 GHz in He [44] gives a de-phasing time of the order of 5×10^{-10} s. Velocity changing collisions have times of the same order of magnitude. RET rates, that also at equilibrium provide a continuous exchange of population, in both states, have a time of the order of 3×10^{-10} s. As a whole, then, and even in pure He, a de-phasing characteristic time of the order of 10^{-10} s can be estimated, that is much less than the pulse rise time. The addition of molecular gases has the effect of reducing the de-phasing time, since it generally increases both the pressure broadening and the quenching rate. A quantitative analysis of the difference between DME and RE model outcomes, reported in [79], confirmed these results. In addition, the RE formulation, in conditions of sufficiently fast de-phasing as in our case, and in the presence of quenching, was seen to decrease its accuracy on increasing electric field strength and on increasing the electronic quenching up to values comparable to the pulse duration, but always with a reasonable error never larger than about 15% [79]. For this reason, anyway, the choice of working at moderate saturation conditions is a conservative one.

All the previous discussion refers to a single-mode laser. Our laser is, instead, a multi-mode one, with a variable composition of 3-5 modes per pulse, and rare pulses with 2 modes only. Modes are totally uncorrelated between each other, so that the interaction of a molecule with such a multi-mode field implies a series of photon exchanges that may not be in phase. This subject is quite difficult to treat, but certainly we can state qualitatively that it is a further source of de-phasing, at the limit of thermal light interaction when the number of modes is large, giving further validity to the RE approach. In [80] and references therein, it was stated that the RE approach is valid if the coherence time of the laser is short compared to the pumping time (reciprocal of absorption probability).

9.2. Appendix b: spectral overlap integral

The spectral overlap of the laser line and the absorption line is calculated as follows. We define the spectral quantities:

$$\mathcal{E}_\nu(t, \nu) = \mathcal{E}_L(t)\varepsilon(\nu - \nu_L) \quad \text{with} \quad \int_{-\infty}^{\infty} \varepsilon(\nu - \nu_L)d\nu = 1$$

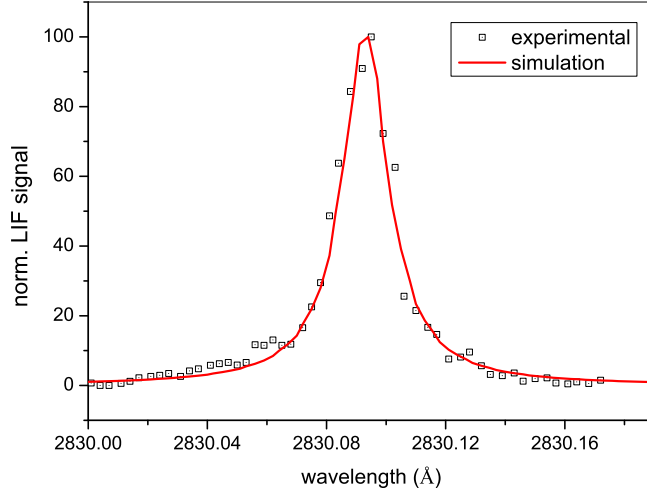


Figure 18. Laser excitation spectrum (laser wavelength scan) of an isolated rovibrational line ($P_1(3)$), with pressure (0.00535 \AA) + Doppler (0.00916 \AA) broadening = 0.0122 \AA . The model simulation is obtained by a Lorentzian laser profile with $9 \times 10^{-3} \text{ \AA}$ width.

$$B_{\nu,x}(\nu) = B_x b(\nu - \nu_x) \quad \text{with} \quad \int_{-\infty}^{\infty} b(\nu - \nu_x) d\nu = 1 \quad (12)$$

The subscript x indicates the absorption line. The spectral profile of the laser line, $\varepsilon(\nu)$, has been deduced from the fit of laser excitation spectra (see fig. 18). $b(\nu)$ is given by the Doppler plus pressure broadening. Then:

$$\psi = \int_{-\infty}^{\infty} \varepsilon(\nu - \nu_L) b(\nu - \nu_x) d\nu \quad (13)$$

The superposition of $\varepsilon(\nu - \nu_L)$ and $b(\nu - \nu_x)$ is shown in Figure 19, where the laser is tuned on the $P_1(3)$ line. Note finally that the product $\mathcal{E}_L(t)\psi$ has the correct dimensions of a spectral radiant energy density required for multiplication with the Einstein coefficient B .

9.3. Appendix c: laser beam spatial distribution treatment

First we point out that the functional dependence of equation 10 is normally used in textbooks for the electric field of a gaussian beam, implying for energy related quantities the form $\exp(-2r^2/w_0^2)$, i.e. still a gaussian with half the waist of the electric field. We have chosen equation 10, as in [50], since any method for visualizing the beam, being it a trace on photographic paper or a true measurement, is sensitive to the energy, not to the electric field, so that w_0 is more immediately correlated to the measured/estimated beam size. Integrating equation 10 over r and over the whole 2π angle we get that the energy within a circle of radius R is:

$$E_R = E_{las} \times [1 - \exp(-R^2/w_0^2)] \quad (14)$$

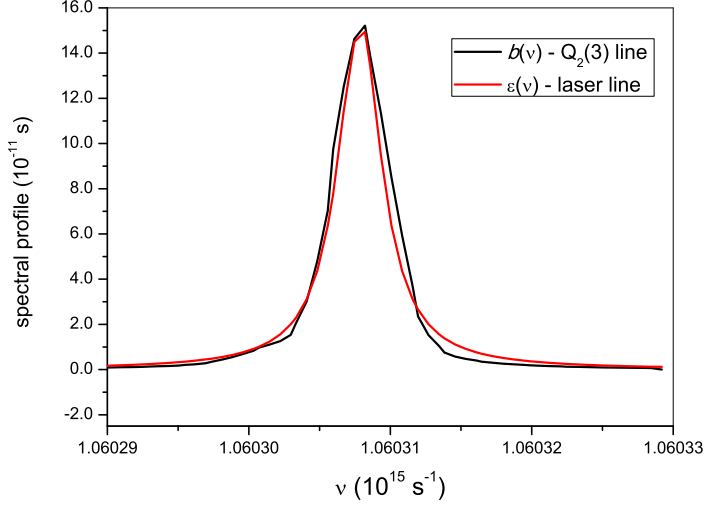


Figure 19. Spectral absorption and laser line profiles with the laser tuned on the $P_1(3)$ line. In this case $\psi = 8.65 \times 10^{-11} s$

so that the energy flowing through the annulus with surface $S_{1,2}$ enclosed within the radii R_1 and R_2 is:

$$E_{1,2} = E_{las} \times [\exp(-R_1^2/w_0^2) - \exp(-R_2^2/w_0^2)] \quad (15)$$

$$S_{1,2} = \pi(R_2^2 - R_1^2) \quad (16)$$

With this distribution we have a central region, (circle with $r \leq w_0$) with 63.2 % of the energy, an intermediate region (annulus with $w_0 \leq r \leq 2w_0$) with 35 % of the energy, and a peripheric region ($r \geq 2w_0$) with 1.8 % of the energy. We treat the calculation with a gaussian beam as follows. We discretize the radius into 17 values up to $3.4 \times w_0$. For each annulus we solve numerically the model 6, with a radiant energy density given by

$$\mathcal{E}_L^{(i,i+1)} = W(t)[\exp(-R_i^2/w_0^2) - \exp(-R_{i+1}^2/w_0^2)]/(cS_{i,i+1}) \quad (17)$$

and we then sum up the model outcomes over all the annula ($P_{i,i+1}$), weighted by a number proportional to the sampled volume fraction:

$$P_{A1}(t) = \sum_{i=0}^{16} P_{i,i+1} S_{i,i+1} / (\pi w_0^2) \quad (18)$$

The volume fraction is equal to the surface fraction, the other dimension being determined by the slit width. Normalization to the waist surface makes this factor adimensional and loads the sampled volume into the calibration constant. In practice at large radii, although the energy is very low, the contribution to the LIF outcome is still significant due to the larger volume fraction. This is particularly true when the energy is large, and the beam core is highly saturated.

10. References

- [1] Lu X, Laroussi M and Puech V 2012 *Plasma Sources Sci. and Technol.* **21** 034005
- [2] Lu X, Naidis G, Laroussi M and Ostrikov K 2014 *Phys. Rep.* **540** 123 – 166 ISSN 0370-1573 guided ionization waves: Theory and experiments
- [3] von Woedtke T, Reuter S, Masur K and Weltmann K D 2013 *Phys. Rep.* **530** 291 – 320 ISSN 0370-1573 plasmas for Medicine
- [4] De Benedictis S and Dilecce G 2013 *Physics and technology of atmospheric pressure discharges* (Taylor and Francis) chap Laser-Induced Fluorescence Methods for Transient Species Detection in High-Pressure Discharges, pp 261–284
- [5] Dilecce G, Ambrico P F and De Benedictis S 2010 *Journal of Physics D: Applied Physics* **43** 124004
- [6] Dilecce G, Ambrico P F, Scarduelli G, Tosi P and De Benedictis S 2009 *Plasma Sources Sci. Technol.* **18** 015010
- [7] Dilecce G, Ambrico P F and De Benedictis S 2007 *Plasma Sources Sci. Technol.* **16** 511 – 522
- [8] van Gessel A F H, Alards K M J and Bruggeman P J 2013 *J. Phys. D: Appl. Phys.* **46** 265202
- [9] Schmidt J B, Jiang N and Ganguly B N 2014 *Plasma Sources Sci. Technol.* **23**
- [10] Ono R and Oda T 2002 *J. Phys. D: Appl. Phys.* **35** 2133 – 2138
- [11] Ono R and Oda T 2003 *J. Appl. Phys.* **93** 5876–5882
- [12] Kanazawa S, Tanaka H, Kajiwara A, Ohkubo T, Nomoto Y, Kocik M, Mizeraczyk J and Chang J S 2007 *Thin Solid Films* **515** 4266 – 4271
- [13] Kanazawa S, Kawano H, Watanabe S, Furuki T, Akamine S, Ichiki R, Ohkubo T, Kocik M and Mizeraczyk J 2011 *Plasma Sources Sci. Technol.* **20** 034010
- [14] Nakagawa Y, Ono R and Oda T 2011 *J. Appl. Phys.* **110** 073304
- [15] Magne L, Pasquiers S, Blin-Simiand N and Postel C 2007 *J. Phys. D: Appl. Phys.* **40** 3112 – 3127
- [16] Dilecce G, Ambrico P F, Simek M and De Benedictis S 2012 *Chem. Phys.* **398** 142–147
- [17] Dilecce G and De Benedictis S 2011 *Plasma Phys. Controlled Fusion* **53** 124006
- [18] Teramoto Y, Kim H H, Ogata A and Negishi N 2014 *J. Appl. Phys.* **115** 133302
- [19] Srivastava N and Wang C 2011 *J. Appl. Phys.* **110** 053304
- [20] Xiong Q, Nikiforov A Y, Li L, Vanraes P, Britun N, Snyders R, Lu X P and Leys C 2012 *Eur. Phys. J. D* **66** 281
- [21] Yonemori S, Nakagawa Y, Ono R and Oda T 2012 *J. Phys. D: Appl. Phys.* **45** 225202
- [22] Vorac J, Dvorak P, Prochazka V, Ehlbeck J and Reuter S 2013 *Plasma Sources Sci. Technol.* **22** 025016
- [23] Pei X, Lu Y, Wu S, Xiong Q and Lu X 2013 *Plasma Sources Sci. Technol.* **22** 025023
- [24] Vorac J, Obrusn A, Prochazka V, Dvoak P and Talaba M 2014 *Plasma Sources Sci. Technol.* **23** 025011
- [25] Pei X, Wu S, Xian Y, Lu X and Pan Y 2014 *IEEE Trans. Plasma Sci.* **14**
- [26] Verreycken T, van der Horst R M, Baede A H F M, Van Veldhuizen E M and Bruggeman P J 2012 *J. Phys. D: Appl. Phys.* **45** 045205
- [27] Verreycken T and Bruggeman P J 2014 *Plasma Sources Sci. Technol.* **23** 015009
- [28] Verreycken T and Bruggeman P J 2014 *Plasma Chem. Plasma Process.* **34** 605 – 619
- [29] Choi I, Yin Z, Adamovich I V and Lempert W R 2011 *IEEE Trans. Plasma Sci.* **39** 3288–3299
- [30] Lacoste D A, Xu D A, Moeck J P and Laux C O 2013 *Proceedings of the Combustion Institute* **34** 3259 – 3266 ISSN 1540-7489
- [31] Walsh J L and Kong M G 2008 *Appl. Phys. Lett.* **93** 111501
- [32] Sobolewski M A 1992 *Journal of Vacuum Science & Technology A* **10** 3550–3562
- [33] Hofmann S, van Gessel A F H, Verreycken T and Bruggeman P 2011 *Plasma Sources Sci. Technol.* **20** 065010
- [34] Martini L M, Dilecce G, Scotoni M, Tosi P and De Benedictis S 2014 *Plasma Process. Polym.* **11** 232–238

- [35] Dilecce G, Ambrico P F, Simek M and De Benedictis S 2012 *J. Phys. D: Appl. Phys.* **45** 125203
- [36] Brown J M and ACarrington 2003 *Rotational Spectroscopy of Diatomic Molecules* (Cambridge University Press)
- [37] Herzberg G 1950 *Molecular Spectra and Molecular Structure* (D. Van Nostrand Company Inc.)
- [38] Dieke G H and Crosswhite H M 1962 *J. Quant. Spectrosc. Radiat. Transfer.* **2** 97–199
- [39] Brown J M, Hougen J T, Huber K P, Johns J W C, Kopp I, Lefebvre-Brion P H, Merer A J, Ramsay D A, Rostas J and Zare R N 1975 *J. Mol. Spectrosc.* **55** 500 – 503
- [40] Verreycken T, Sadeghi N and Bruggeman P J 2014 *Plasma Sources Science and Technology* **23** 045005
- [41] Bruggeman P, Cunge G and Sadeghi N 2012 *Plasma Sources Sci. Technol.* **21** 035019
- [42] Riés D, Dilecce G, Robert E, Ambrico P, Dozias S and Pouvesle J M 2014 *J. Phys D: Appl. Phys* in press
- [43] Luque J and Crosley D 1999 Int. rep. p99-009 Tech. rep. SRI
- [44] Kasyutich V L 2005 *Eur. Phys. J. D* **33** 29 – 33
- [45] Cybulski H, Bielski A, Ciury R, Szudy J and Trawinski R S 2013 *J. Quant. Spectr. Rad. Transfer* **120** 90 – 103 ISSN 0022-4073
- [46] Verreycken T, Mensink R, van der Horst R, Sadeghi N and Bruggeman P J 2013 *Plasma Sources Sci. Technol.* **22** 055014
- [47] Dunn M J and Masri A R 2010 *Appl. Phys. B* **101** 445 – 463
- [48] Luque J, Klein-Douwel R J H, Jeffries J B, Smith G P and Crosley D R 2002 *Appl. Phys. B* **75** 779 – 790
- [49] Verreycken T, van der Horst R M, Sadeghi N and Bruggeman P J 2013 *J. Phys. D: Appl. Phys.* **46** 464004
- [50] Daily J W 1978 *Appl. Opt.* **17** 225–229
- [51] Lengel R K and Crosley D R 1978 *J. Chem. Phys.* **68** 5309–5324
- [52] Williams L R and Crosley D R 1996 *J. Chem. Phys.* **104** 6507–6514
- [53] Copeland R A, Dyer M J and Crosley D R 1985 *J. Chem. Phys.* **82** 4022–4032
- [54] Burris J, J J Butler J, T J McGee T and W S Heaps W 1988 *Chem. Phys.* **124** 251 – 258
- [55] Copeland R A, Wise M L and and D R C 1988 *J. Phys. Chem.* **92** 5710
- [56] German K R 1976 *J. Chem. Phys.* **64** 4065–4068
- [57] Wysong I J, Jeffries J B and Crosley D R 1990 *J. Chem. Phys* **92** 5218–5222
- [58] Bailey A E, Heard D E, Henderson D A and Paul P H 1999 *Chem. Phys. Lett.* **302** 132 – 138
- [59] German K R 1975 *J. Chem. Phys.* **63** 5252
- [60] Jorg A, Degli Esposti A and Werner H J 1990 *J. Chem. Phys.* **93** 8757
- [61] Jorg A, Maier U and Kohse-Hoinghaus K 1990 *J. Chem. Phys.* **93** 6453
- [62] Kienle R, Jorg A and Kohse-Hoinghaus K 1993 *Appl. Phys. B* **56** 249 – 258
- [63] Zizak G, Petrucci G A, Stevenson C L and Winefordner J D 1991 *Appl. Opt.* **30** 32611 – 32046
- [64] Tobai J, Dreier T and Daily J W 2002 *J. Chem. Phys.* **116** 4030–4038
- [65] Katayama D H 1986 *J. Chem. Phys.* **84** 1477
- [66] Lee S, Luque J, Reppel J, Brown A and Crosley D R 2004 *J. Chem. Phys.* **121** 1373
- [67] Crichton H, Murray C and McKendrick K 2002 *Physical Chemistry Chemical Physics* **4** 5768
- [68] Wang C C, Chin T L and Lin K C 1997 *J. Chem. Phys.* **107** 10348
- [69] Huang H Y, Tsai M T and Lin K C 2006 *J. Chem. Phys.* **124** 144302
- [70] Cooper J L and Whitehead J C 1994 *J. Phys. Chem.* **98** 8274 – 8278
- [71] Randall C J, Murray C and McKendrick K G 2000 *Phys. Chem. Chem. Phys.* **2** 461 – 471
- [72] Dilecce G, Ambrico P F and De Benedictis S 2006 *Chem. Phys. Lett.* **431** 241 – 246
- [73] Tamura M, Berg P A, Harrington J E, Luque J, Jeffries J B, Smith G P and Crosley D R 1998 *Combust. Flame* **114** 502 – 514
- [74] Bennett K and Byer R 1980 *Appl. Opt* **19** 2408–2412
- [75] Dilecce G 2014 *Plasma Sources Sci. Technol.* **23** 015011
- [76] Yin Z, Montello A, Carter C D, Lempert W R and Adamovich I V 2013 *Combust. Flame* **160**

1594–1608

[77] Loudon R 2000 *Quantum theory of light* (Oxford University Press)

[78] Daily J W 1977 *Appl. Opt.* **16** 2322–2327

[79] Settersten T and Linne M 2002 *J. Opt. Soc. Am. B* **19** 954–964

[80] Avan P and Cohen-Tannoudji C 1977 *J. Phys. B:At. Mol. Phys.* **10** 155–170